# Cyclic muscle contractions reinforce the acto-myosin motors and mediate the full elongation of *C. elegans* embryo

**Anna Dai**[1] **and Martine Ben Amar**[1*]

***For correspondence:**
martine.benamar@phys.ens.fr (MBA)

[1]Laboratoire de Physique de l'Ecole normale supérieure, ENS, Université PSL, CNRS, Sorbonne Université, Université Paris Cité, F-75005 Paris, France

**Abstract** The paramount importance of mechanical forces in morphogenesis and embryogenesis is widely recognized, but understanding the mechanism at the cellular and molecular level is still challenging. Due to its simple internal organization, Caenorhabditis elegans is a worthwhile study system. As demonstrated experimentally, after a first period of steady elongation due to the acto-myosin network, muscle contractions operate a quasi-periodic sequence of bending, rotation and torsion, which leads to the final 4-fold size of the embryo before hatching. How acto-myosin and muscles contribute to embryonic elongation is herein theoretically studied. A filamentary elastic model that converts stimuli generated by biochemical signals in the tissue into driving forces, explains embryonic deformation under actin bundles and muscle activities, and dictates mechanisms of late elongation based on the effects of energy conversion and dissipation. We quantify this dynamic transformation by stretches applied to a cylindrical structure mimicking the body shape in finite elasticity, obtaining good agreement and understanding for both wild-type and mutant embryos at all stages.

## Introduction

Mechanical stresses play a critical role during embryogenesis, affecting complex biological tissues such as the skin, the brain, and the interior of organs. There are many studies in the last decades, for example, the pattern of the intestine (***Coulombre and Coulombre*** (***1958***); ***Hannezo et al.*** (***2011***); ***Li et al.*** (***2011***); ***Ben Amar and Jia*** (***2013***); ***Shyer et al.*** (***2013***)), the brain cortex (***Toro and Burnod*** (***2005***); ***Goriely et al.*** (***2015***); ***Ben Amar and Bordner*** (***2017***); ***Tallinen et al.*** (***2016***)), and the circumvolutions of the fingerprints (***Kücken and Newell*** (***2005***); ***Ciarletta and Ben Amar*** (***2012***)) that have been interpreted as the result of compressive stresses generated by growth occurring a few months post fertilization for humans. At a smaller scale, the influence of mechanical stresses superposed to cellular processes (e.g., division, migration) and tissue organization becomes more complex to be identified and quantified. For example, independently of growth, stresses may be generated by different molecular motors, among which myosin II, linked to actin filaments, is the most prevalent during epithelial cell morphogenesis (***Vicente-Manzanares et al.*** (***2009***)) and cell motility (***Cowan and Hyman*** (***2007***); ***Olson and Sahai*** (***2009***); ***Palumbo et al.*** (***2022***)). The spatial distribution and dynamics of myosin II greatly influence the morphogenetic process (***Levayer and Lecuit*** (***2012***); ***Lv et al.*** (***2022***)), as demonstrated for Drosophila (***Bertet et al.*** (***2004***); ***Blankenship et al.*** (***2006***); ***Saxena et al.*** (***2014***); ***Shindo and Wallingford*** (***2014***)) and also *C. elegans* embryo (***Priess***

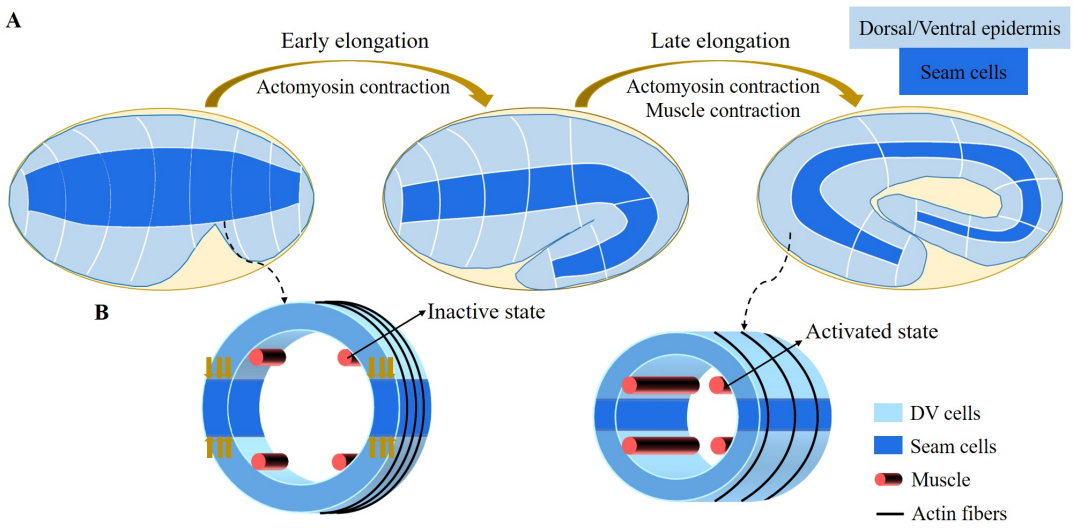


**Figure 1.** (A) Overview of *C. elegans* embryonic elongation. Three epidermal cell types are found around the circumference: dorsal, ventral and lateral. (B) Schemes showing a *C. elegans* cross-section of the embryo. Small yellow arrows in the left image indicate the contraction force that occurred in the seam cell. Four muscle bands underneath the epidermis and actin bundles surround the outer epidermis.

***and Hirsh*** (***1986***); ***Gally et al.*** (***2009***); ***Ben Amar et al.*** (***2018***)).

The embryonic elongation of *C. elegans* represents an attractive model of matter reorganization without a mass increase before hatching. It happens after the ventral enclosure and takes around 240 minutes to convert the lima-bean-shaped embryo into a final elongated worm shape: the embryo elongates along the anterior/posterior axis by four times (***McKeown et al.*** (***1998***)). The short lifetime of the egg before hatching and its transparency makes this system an ideal system to study the forces that exist in the cortical epithelium or its vicinity. However, unlike the embryonic development of Drosophila and Zebrafish, there is neither cell migration, cell division nor a notable change in embryonic volume (***Sulston et al.*** (***1983***); ***Priess and Hirsh*** (***1986***)), only a noticeable epidermal elongation drives the whole morphogenetic process of *C. elegans* in the period post enclosure. There are two experimentally identified driving forces for the elongation: the actomyosin contractility in seam cells of the epidermis, which seems to last during the whole elongation process, and the muscle activity beneath the epidermis that starts after the $1.7 \sim 1.8$-fold stage. The transition is well defined since the muscle participation makes the embryo rather motile impeding any physical experiments such as laser ablation, which could be conducted and achieved in the first period (***Vuong-Brender et al.*** (***2017a***)). Consequently, the elongation process of *C. elegans* could be divided into two stages: the early elongation and the late elongation, depending on the muscle activation, and Fig.1(A) shows the whole elongation process (***Vuong-Brender et al.*** (***2017a***)). Previously, the role of the actomyosin network in the seam cells during the early elongation of *C. elegans* was investigated (***Ben Amar et al.*** (***2018***)). Based on the geometry of a hollow cylinder composed of four parts (seam and dorso-ventral cells), a model involving the pre-stress responsible for the enclosure, the active compressive ortho-radial stress joined to the passive stress quantitatively predicts the elongation, but only up to $\sim 70\%$ of the initial length.

For the late elongation phase, the acto-myosin network and muscles drive together the full elongation during this phase (***Vuong-Brender et al.*** (***2017a***)). Muscles play an important role since mutants with muscle defects are unable to complete the elongation process, even though the acto-myosin network operates normally (***Lardennois et al.*** (***2019***)). Fig.1(B) shows the schematic image of *C. elegans* body (***Zhang et al.*** (***2011***)) with four rows of muscles, two of which are underneath the dorsal epidermis and the other two are under the ventral epidermis. As observed *in vivo*, *C. elegans*

exhibits systematic rotations accompanying each contraction (***Yang*** (***2017***); ***Yang Xinyi et al.*** (***2023***)), and deformations such as bending and twisting. Eventually, the *C. elegans* embryo will complete an elongation from $1.8$-fold to $4$-fold. We can imagine that once the muscle is activated on one side, it can only contract, and then the contraction forces will be transmitted to the epidermis on this side. So one can wonder how an elongation can occur since striated muscles can only perform cycles of contraction and relaxation, their action will tend to reduce the length of the embryo. Therefore, it is necessary to understand how the embryo elongates during each contraction and how the muscle contractions couple to the acto-myosin activity. This work aims to answer this paradox within the framework of finite elasticity without invoking cell plasticity and stochasticity which cannot be considered driving forces. In addition, several important issues at this stage remain unsettled. First of all, we may also observe a torsion of the embryo but if the muscle activity suggests a bending, it cannot explain alone a substantial torsion. Secondly, a small deviation of the muscle axis (***Moerman and Williams*** (***2006***)) is responsible for a series of rotations, how to relate these rotations to the muscle activation (***Yang*** (***2017***)). Since any measurement on a motile embryo at this scale is difficult, it is meaningful to explore the mechanism of late elongation theoretically. Furthermore, muscle contraction is crucial in both biological development and activities and has been studied extensively by researchers (***Tan and De Vita*** (***2015***); ***De Vita et al.*** (***2017***)), but how it works at small scales remains a challenge.

Using a finite elasticity model and assuming the embryonic body shape is cylindrical, we can evaluate the geometric bending deformation and the energy released during each muscular contraction on one side since after each contraction, the muscles relax and then muscles on the opposite side undergo a new contraction. This cyclic process leads to a tiny elongation of the cylinder along its symmetry axis at each contraction. Each of them is correlated with the rotational movements of the embryo (***Yang*** (***2017***)). By repeating these pairs of contractions more than two hundred times, a cumulative extension is achieved, but it must be reduced by friction mechanisms, also evaluated by the model. Furthermore, the mechanical model explains the existence of a torque operating at the position of the head or tail by the coupling of muscle contraction with the orthoradial acto-myosin forces. Finally, the small deviation between the muscles and the central axis experimentally detected (***Moerman and Williams*** (***2006***)) induces cyclic rotations and possibly torsion leading to fluid viscous flow inside the egg. Quantifying all these processes allows evaluating the physical quantities of the embryo such as the shear modulus of each component, the osmolarity of the interstitial fluid and the active forces exerted by the acto-myosin network and the muscles which are sparsely known in the embryonic stages.

Our mechanical model accounts for the dynamical deformations induced by the internal stimuli of a layered soft cylinder, enabling us to make accurate quantitative predictions about the active networks of the embryo. Furthermore, our model takes into consideration the dissipation that occurs in the late period just before the egg hatch. Our results are consistent with observations of acto-myosin and muscle activity (***Vuong-Brender et al.*** (***2017a***); ***Ben Amar et al.*** (***2018***); ***Lardennois et al.*** (***2019***)). The architecture of our paper is illustrated in Fig.2.

## Results

It is widely recognized that *C. elegans* is a well-established model organism in the field of developmental biology. However, it is less widely known that its internal striated muscles share similarities with skeletal muscles found in vertebrates in terms of both function and structure (***Lesanpezeshki et al.*** (***2021***)). Being contractile, the role of the four axial muscles (as shown in Fig.1) in the final shaping of the embryo is nearly contra-intuitive. In this section, we aim to highlight the action of these muscles when coupled to the acto-myosin network, using a purely mechanical approach. To achieve a quantitative understanding, our method requires a detailed description of the deformation geometry of the embryo, with the body shape represented by a fully heterogeneous cylinder.

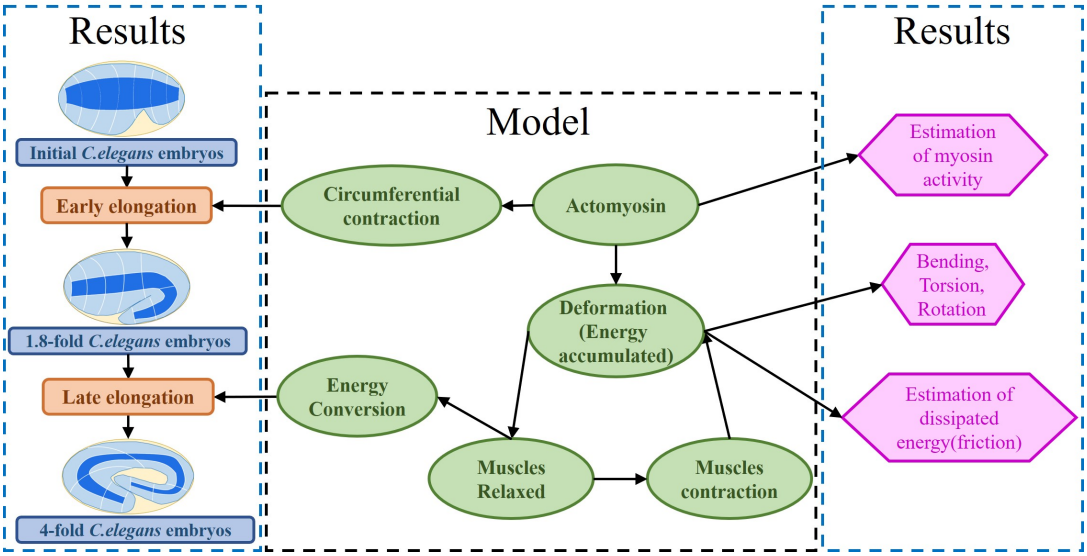


**Figure 2.** Architecture of the program. The program reflects the framework of research. On the one hand, the proposed model explains the early and late elongation of the *C. elegans*, on the other hand, the early myosin activity is estimated, the deformations (bending, twisting, rotation) happening in the late period is recovered, and the estimation of energy dissipated during muscle activity is achieved.

## Geometric and strain deformations of the embryo

The early elongation of *C. elegans* embryo was previously studied, which is characterized by an inner cylinder surrounded by epithelial cells located in the cortical position (***Ben Amar et al.*** (***2018***)). The cortex is composed of three distinct cells - the seam, dorsal, and ventral cells - which exhibit unique cytoskeleton organization and actin network configurations. Among these, only the seam cells possess active myosin motors that function in the ortho-radial direction, allowing for the contraction of the circumference and thereby triggering the early elongation process. In this study, we simplify the cylindrical geometry of the body and treat the epidermis as a unified whole with effective activity localized along the circumference, supported by four muscles distributed beneath the epidermis. Muscles play no role in the early elongation stage so were not considered previously (***Vuong-Brender et al.*** (***2017a***); ***Ben Amar et al.*** (***2018***)). After this period of approximately a 1.8-fold increase in length, muscles parallel to the main axis and actin bundles organized along the circumference will collaborate to facilitate further elongation. Table. 1 provides the size parameters of *C. elegans* which will be introduced hereafter.

**Table 1.** Adopted real size parameters of the *C. elegans* (***Vuong-Brender et al.*** (***2017a***); ***Ben Amar et al.*** (***2018***)).

| | Initial | 1.8-fold |
|---|---|---|
| Radius | 11.1 $\mu m$ | 8.2 $\mu m$ |
| Length | 50 $\mu m$ | 90 $\mu m$ |

We focus on the overall deformation of a full cylinder or a thin rod, having a length $L$ greater than the radius $R$ and a central vertical axis along the $Z$ direction. Contrary to previous works (***Ciarletta et al.*** (***2009***); ***Ben Amar et al.*** (***2018***)), here we decide to simplify the geometrical aspect because of the mechanical complexity. The biological activity induced by the acto-myosin network and muscles is represented by active strains, and the global shape is the result of the coupling between elastic and active strains, modulated by dissipation. Active strains are generated through non-mechanical processes (e.g., biochemical processes): myosin motors and striated muscles receive their energy from ATP hydrolysis, which is converted to mechanical contractions of fibers.

Due to the significant deformation observed, the central line is distorted and becomes a curve in three-dimensional space, represented by a vector $\mathbf{r}(\mathbf{Z})$, as depicted in Fig.3(A). Along this curve, perpendicular planar sections of the embryo can be defined, and the deformation in each section can be quantified since the circular geometry is lost with the contractions (***Kaczmarski et al.*** (***2022***)). The geometric mapping is as follows:

$$\chi(\mathbf{X}) = \mathbf{r}(Z) + \sum_{i=1}^{3} \varepsilon a_i(\varepsilon R, \Theta, Z)\, \mathbf{d}_i(Z), \tag{1}$$

where the $a_i$ represents the deformation in each direction of the section with $a_i(0,0,Z) = 0$ so that the $Z$-axis maps to the centerline $\mathbf{r}(Z)$. The small quantity $\varepsilon$ is the ratio between the radius $R$ and the length $L$ of the cylinder. Referring to the model proposed by B. Kaczmarki *et al*. (***Kaczmarski et al.*** (***2022***)), we define the initial configuration $\mathcal{B}_0$ with material points $(X, Y, Z)$, and the mapping function $\chi(\mathbf{X})$ links the initial configuration $\mathcal{B}_0$ to the current configuration $\mathcal{B}$. The geometric deformation gradient is $\mathbf{F} = \text{Grad}\chi = \mathbf{F_e G}$ (***Nardinocchi and Teresi*** (***2007***)), where $\mathbf{G}$ represents the active strain generated by the actomyosin or the muscles, and $\mathbf{F_e}$ is the elastic strain tensor. Because of the two stages through which the *C. elegans* elongates, we need to evaluate the influence of the *C. elegans* actin network during the early elongation before studying the deformation at the late stage. So, the deformation gradient can be decomposed into: $\mathbf{F} = \mathbf{F}_e\mathbf{G}_1\mathbf{G}_0$ (***Goriely and Ben Amar*** (***2007***)) where $\mathbf{G}_0$ refers to the pre-strain of the early period and $\mathbf{G}_1$ is the muscle-actomyos in supplementary active strain in the late period. Actin is distributed in a circular pattern in the outer epidermis, see Fig.3(B), so the finite strain $\mathbf{G}_0$ is defined as $\mathbf{G}_0 = Diag\left(1, g_0(t), 1\right)$, where $0 < g_0 < 1$ is the time-dependent decreasing eigenvalue, operating in the actin zone and is equal to unity in the other parts: $g_0(0) = 1$. In the case without pre-strain, $\mathbf{G}_0 = \mathbf{I}$. The deformation gradient follows the description of Eq.(1) :$\mathbf{F} = F_{ij}\mathbf{d}_i \otimes \mathbf{e}_j$, $i \in \{1,2,3\}$ and $j \in \{R, \Theta, Z\}$.

When considering a filamentary structure with different fiber directions $\mathbf{m}$, these directions are specified by two angles $\alpha$ and $\beta$, as outlined in (***Holzapfel*** (***2002***)): $\mathbf{m} = \sin\alpha\sin\beta\,\mathbf{e_R} + \sin\alpha\cos\beta\,\mathbf{e_\Theta} + \cos\alpha\,\mathbf{e_Z}$, $\alpha, \beta \in \left[-\pi/2, \pi/2\right]$, where $\alpha$ and $\beta$ lie in the range $[-\pi/2, \pi/2]$. For muscle fibers, $\alpha_m = 0$ and $\beta_m = 0$, whereas for hoop fibers in the actin network, $\alpha_a = \pi/2$ and $\beta_a = 0$. When the muscles are activated and bend the embryo, the actin fibers become inclined with a slope $\alpha$, such that $-\pi/2 < \alpha_a < \pi/2$, $\alpha_a \neq 0$, and $\beta_a = 0$. Each active strain is represented by a tensor $\mathbf{G_i} = \mathbf{I} + \varepsilon \mathbf{g_i m_i} \otimes \mathbf{m_i}$, where $g_i$ represents the activity ($g_m$ for the muscles and $g_a$ for acto-myosin), and since both are contractile, their incremental activities are negative. Additional calculation details are provided in Section Methods and Materials.

To relate the deformations to the active forces induced by muscles and the acto-myosin network, we assume that the embryo can be represented by the simplest nonlinear hyperelastic model, called Neo-Hookean, with a strain-energy density given by $W\left(\mathbf{F}_e\right) = \frac{\mu}{2}\left(tr\left(\mathbf{F}_e\mathbf{F}_e^{\,T}\right) - 3\right)$. In cylindrical coordinates, the total energy of the system and the auxiliary energy density is:

$$\begin{aligned} W &= \varepsilon^2 \int_0^L \mathrm{d}Z \int_S V(\mathbf{F}_e, \mathbf{G}) R\, \mathrm{d}R\, \mathrm{d}\Theta, \\ V &= W(\mathbf{F_e}) - p(J-1). \end{aligned} \tag{2}$$

where $J = \det \mathbf{F}_e$, $p$ is a Lagrange multiplier which ensures the incompressibility of the sample, a physical property assumed in living matter. When the cylinder involves several layers with different shear modulus $\mu$ and different active strains, the integral over $S$ covers each layer. To minimize the energy over each section for a given active force, we take advantage of the weakness of $\varepsilon$ and expand the inner variables $a_i$, $p_i$, and the potential $V$ to obtain the auxiliary strain-energy density. Given that the Euler-Lagrange equations and the boundary conditions are satisfied at each order, we can obtain solutions for the elastic strains at zero order $\mathbf{a}^{(0)}$ and at first order $\mathbf{a}^{(1)}$. Finally, these solutions which will represent a combination of bending and torsion deformation will last the time of a muscle contraction while the acto-myosin will continue its contractile activity. The evaluation

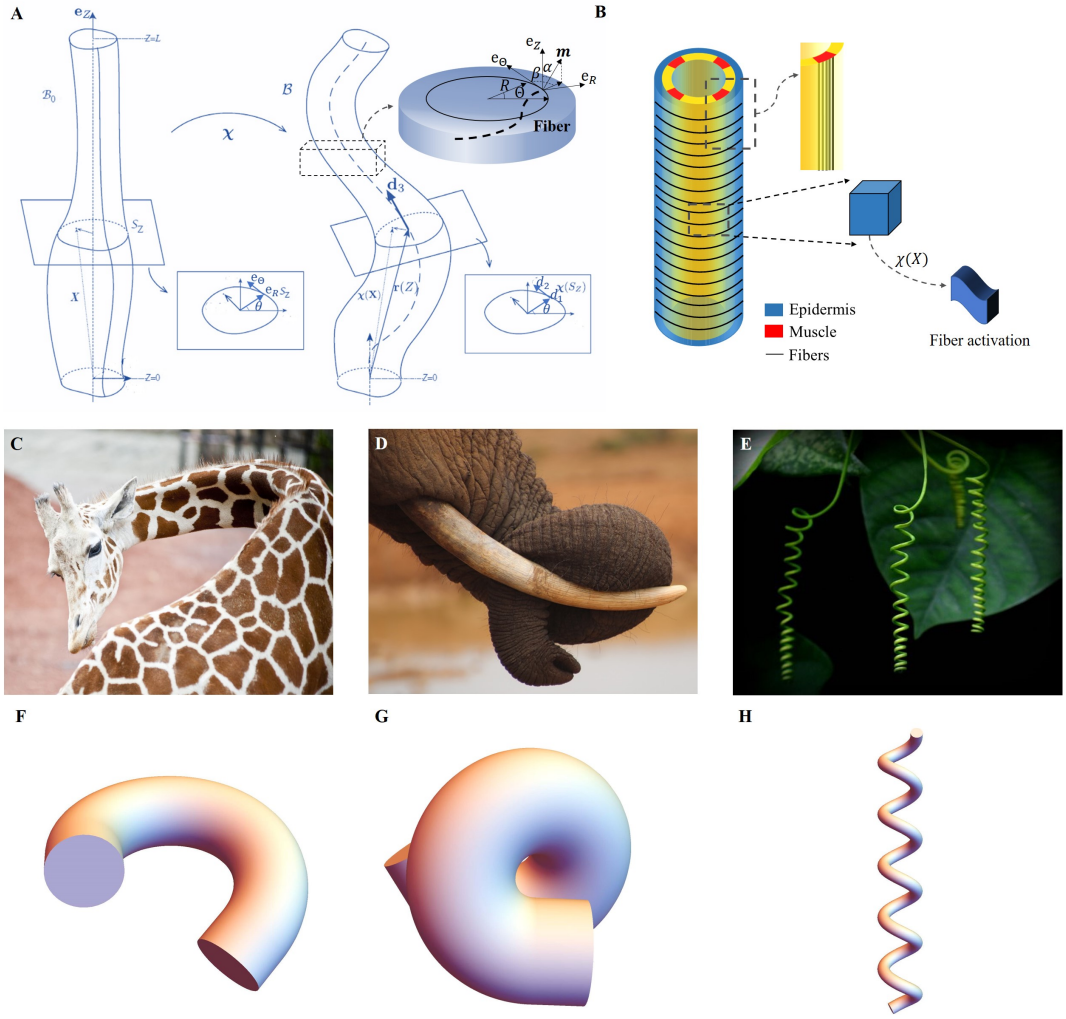


**Figure 3.** (A) Cylindrical structure in the reference configuration (left) with a vertical central axis and its deformation in the current configuration (right). The deformed configuration is fully parameterized by the centerline $\mathbf{r}(Z)$ (resulting from the distortion of the central axis) and the deformation of each cross-section. (B) Schematic representation of the body shape of the *C. elegans* embryo with the cortical epidermis and the four muscles. The fibers are embedded in the cortex. The blue part representing the epidermis shows the outer distribution of the actin organized into horizontal hoop bundles when the muscles are not activated. The yellow part includes the vertical red muscles, represented by axial fibers. (C) Bending of a Giraffe neck. (D) Torsion of an Elephant trunk. (E) Plant vine twisting. (F) to (H) Deformation configuration under different activations obtained by our simulations for bending and torsion of large rods, twisting and torsion of thin rods.

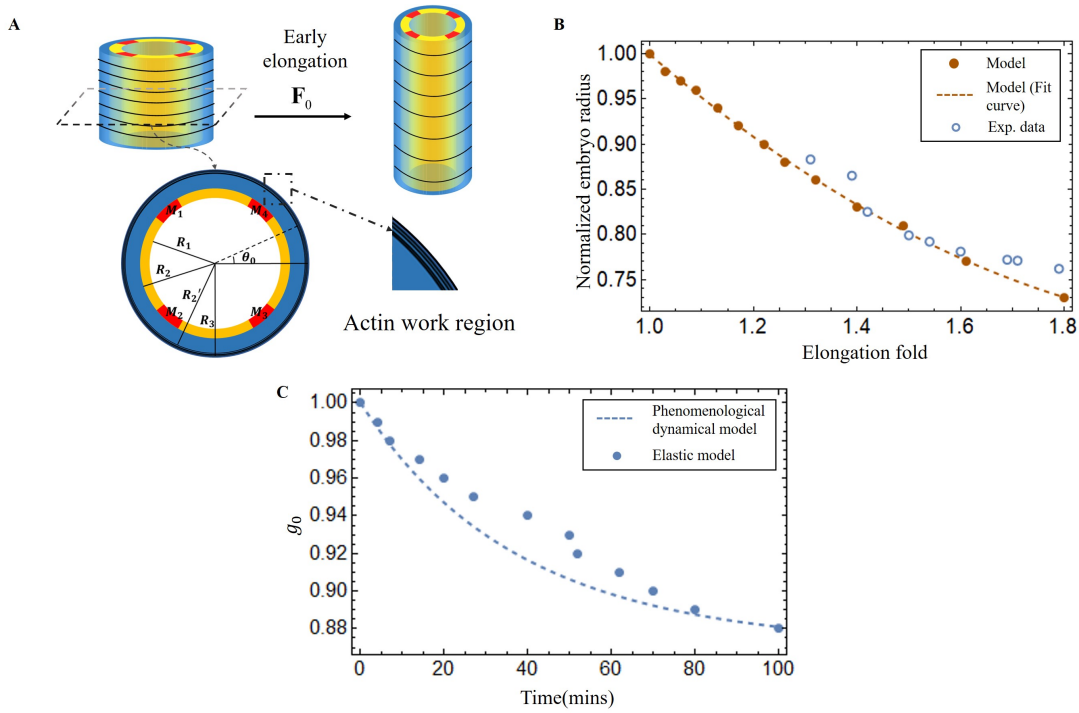


**Figure 4.** (A) The schematic of early elongation and the cross-section of *C. elegans*. In the cross-section, the black circled part is the actin region ($R_2{}' < R < R_3$, with shear modulus $\mu_a$), and the blue part is the epidermis layer ($R_2 < R < R_2{}'$, shear modulus $\mu_e$). The central or inner part ($0 < R < R_2$, shear modulus $\mu_i$) except the muscles which are stiffer. (B) Predictions of normalized embryo radius evolution during early elongation by the pre-strain model compared with experimental data from (***Vuong-Brender et al.*** (***2017a***)). For the model, please refer the Eq.(20) in Appendix 2. (C) Blue dots: extraction of the parameter $g_0(t)$ from Eq.(30) and Eq.(32) in the Appendix 2. Blue dash line, refer to the Eq.(3).

of the elastic energy under acto-myosin-muscle activity at order $\varepsilon^4$ can be compared with the equivalent energy of an extensible elastic rod and each basic deformation will be identified (***Kirchhoff and Hensel*** (***1883***); ***Mielke*** (***1988***); ***Mora and Müller*** (***2002***, 2004); ***Moulton et al.*** (***2020a***)). The typical quantities of interest are the curvature reached during a bending event or a torsion as well as the overall elongation $\zeta$. In the *C. elegans* embryonic system, these quantities result from the competition between the active strains due to muscles and the myosin motors and the elasticity of the body. Similar active matter can be found in biological systems, from animals to plants as illustrated in Fig.3(C)-(E), they have a structure that generates internal stress/strain when growing or activity. Combining anatomy and measurement techniques, we can transform the mechanics of the body under study into a soft sample submitted to localized internal active stresses or localized internal active strains and then deduce its overall deformation mechanisms, some examples are presented in Fig.3(F)-(H).

## The early elongation induced by the acto-myosin

Experimental measurements during the early elongation stage reveal the embryonic diameter and the active or passive stresses, detected by fracture ablation in the body vary with the elongation fold (***Vuong-Brender et al.*** (***2017a***); ***Ben Amar et al.*** (***2018***)). While previous studies have extensively examined this initial stage, we have chosen to revisit it within the context of our geometry, aiming to attain complete control over our structural modeling, encompassing the geometry, shear modulus, and activity of the acto-myosin prior to muscle contraction. At the outset of the second stage, owing to the early elongation, the embryo experiences a pre-strain, which we describe in our model as $\mathbf{G}_0$. The geometry and mechanical information are depicted in Fig.4(A).

Here, we need to first accurately determine $\mathbf{G}_0$ by analyzing the experimental data (***Vuong-Brender et al.*** (***2017a***); ***Ben Amar et al.*** (***2018***)). The cylinder can be divided into three distinct sections: the outer layer is the actin cortex, the thin ring where actin bundles concentrate and work, located within a radius range between $R_2{}'$ and $R_3$ (as shown in Fig.4(A)); the middle layer ($R_2 < R < R_2{}'$), which is the epidermis but without actin; and the inner part ($0 < R < R_2$), where the muscle is located, along with some internal organs, tissues, and fluids. So, we treat the outer and middle layers as incompressible, but the inner part as a compressible material, except the muscles. The initial deformation gradient: $\mathbf{F}_0$ =Diag$(r'(R), r(R)/R, \lambda)$, and $\mathbf{G}_0$ = Diag$(1, g_0, 1)$ with $0 < g_0 < 1$ in the actin layer but with $g_0 = 1$ in the part without actin. $\mathbf{G}_0$ represents the circumferential strain exerted by actin during the early elongation and is a slowly varying function of time. $r(R)$ is the radius after early elongation. By applying the principles of radius continuity, radial stress continuity, and incorporating the zero traction condition on the face of the cylinder, we can determine that $g_0 = 0.88$ when the elongation $\lambda = 1.8$, i.e., at the completion of the early elongation. As illustrated in Fig.4(B), the results of our model and the experimental data are in good agreement, this demonstrates the consistency of the geometric and elastic modeling together with the choice of a pre-strain represented by $\mathbf{G}_0$ which gives a good prediction of the early elongation. More details are displayed in Appendix 3.

From the first stage elongation represented by the blue dots and the blue dashed line in Fig.4(C) we can extract the time evolution of the contractile pre-strain $g_0(t_i)$ derived from our elastic model. To explain quantitatively $g_0(t)$, we suggest a phenomenological dynamical approach for the population of active myosin motors. This equation considers the competition between the recruitment of new myosin proteins from the epidermis cytoskeleton necessary to extend the embryo and the debonding of these myosins from the actin cables, which is damped by the compressive radial stress. It reads:

$$\frac{dX_g(t)}{dt} = \left(p_1 - p_2 X_g(t) e^{-p_3 X_g(t)}\right) \frac{t_v}{t_p} \tag{3}$$

with $X_g = 1 - g_0(t)$, $p_1$ is the ratio between the free available myosin population and the attached ones divided by the time of recruitment (given in minutes), while $p_2$ is the inverse of the debonding time of the myosin motors from the cable: $p_2 = 6$ min$^{-1}$. The debonding time increases (or decreases) when the actin cable is in radial compressive (or tensile) stress, see Appendix 3, Eq.(35). $\tau_v$ is the visco-elastic time estimated from laser ablation fracture operated in the epidermis (***Vuong-Brender et al.*** (***2017b***)): $t_v = 6s$ and $\tau_p$ is the time required for the activation of the myosin motors $t_p = 1200s$ (***Howard and Clark*** (***2002***)). This equation is similar to the model derived by Serra *et al* (***Serra et al.*** (***2021***)) for the viscous stress occurring in gastrulation.

Notice that only $p_1$ and $p_3$ must be obtained by comparison of $g_0(t)$ deduced from Eq.(3) with the values deduced from our elastic model. The result of Eq.(3) with $p_1 = 0.6$ and $p_3 = 0.75$ are shown in Fig.4(C) with a rather good agreement.

## Shape of the embryo under muscles and acto-myosin contraction

The regulation of the muscle contraction in *C. elegans* detected experimentally (***Yang*** (***2017***)) indicates a cyclic process, where two muscles contract on one side of the embryo quite simultaneously and then stop, while on the opposite side, the two muscles start their contractions, but only after a delay. Let us consider first that only muscles are active (see the schematic Fig.5(A) for the structure, then (B) and (C) for the bending). In this case, due to the geometry, only a bending deformation occurs on the left for active muscles localized on left and then on the right for the symmetric muscles on right.

To be more quantitative, we assume that the left side muscles are activated during a short period with an active constant strain value $g_m$ in the region $M_1$ and $M_2$, as shown in Fig.5(A)-(B); if the muscles are perfectly vertical, $\alpha_m = \beta_m = 0$ in the initial configuration. In fact, the two muscles on the same side are not always fully in phase and one may present of small delay. For simplification, we assume them are perfectly synchronous. During the full initial period where muscles are not

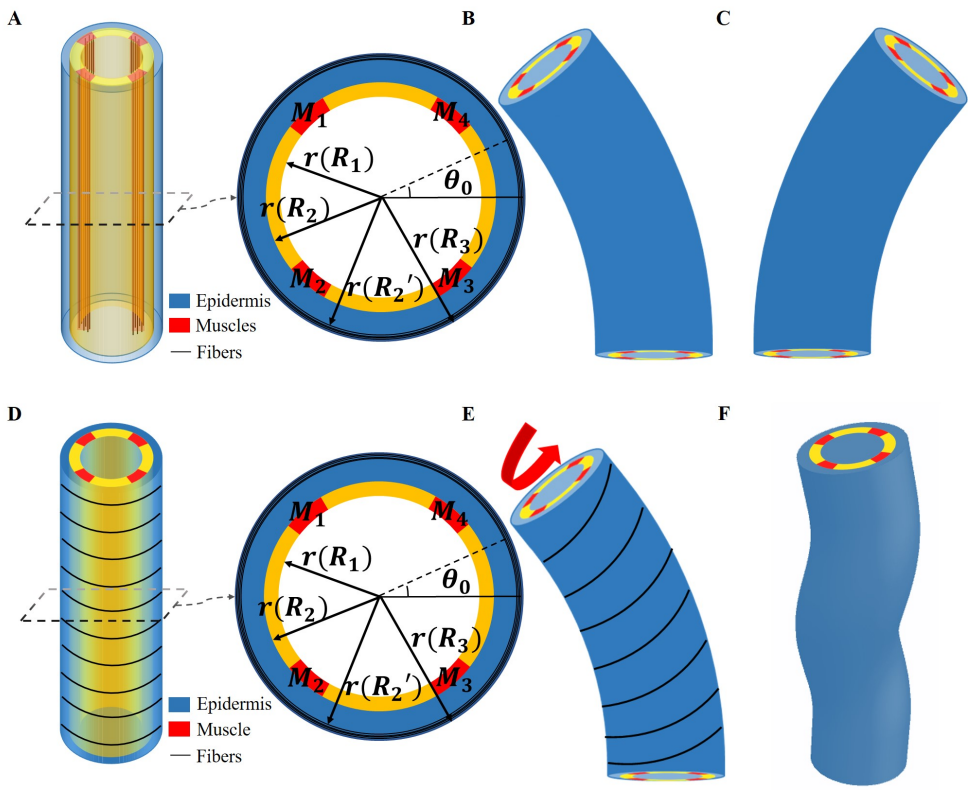


**Figure 5.** (A) Schematic diagram of *C. elegans* muscle fibers and its cross section, and it does not show the actin fibers. Four muscle bands exist in the yellow layer. But, the yellow region is not an actual tissue layer and it is simply to define the position of muscles. (B) Deformation diagram, when left side muscles $M_1(\theta_1 \le \theta_0 \le \theta_2)$ and $M_2(\theta_3 \le \theta_0 \le \theta_4)$. (C) Deformation diagram, when right side muscles $M_3(\theta_5 \le \theta_0 \le \theta_6)$ and $M_4(\theta_7 \le \theta_0 \le \theta_8)$. (D) Schematic diagram of *C. elegans* actin fibers and cross-section. (E) Once the muscle is activated, the actin fiber orientation changes from the 'loop' to the 'slope', which results in torque. (F) Schematic diagram of torsional and bending deformation.

activated, the actin fibers are distributed in a horizontal loop on the outer surface of the epidermis, but once the muscle starts to contract, the acto-myosin network will be re-orientated (***Lardennois et al.*** (***2019***)). The fibers will be then distributed in a sloping pattern causing eventually the twisting of the embryo, see the schematic diagram shown in Fig.5(D)-(F). When this region is activated with a constant strain value, $g_a$, the angle of the actin fibers will change following the amplitude of the bending by the muscle contraction. In this situation, the angle of the actin fibers may change from $\alpha_a \in \left[0, \frac{\pi}{2}\right]$ but $\beta_a$ is not modified and $\beta_a = 0$.

Throughout the entire process, the muscle and acto-myosin activities are assumed to work almost simultaneously. Our modeling allows us to evaluate the bending and torsion generated independently by muscles and actin bundles, culminating in a complete deformation under coupling. Furthermore, the angle of the acto-myosin fibers varies during muscle contractions. We maintain a constant activation of the acto-myosin network and gradually increase muscle activation.

As a result, the bending of the model will be increased, causing a change in the angle of the actin fibers, ultimately yielding a deformation map that is presented in Fig.6(A)-(C). Upon increasing myosin activation, we observed a consistent torsional deformation (Fig.6(E)) that agrees with the patterns seen in the video (Fig.6(D)). However, significant torsional deformations are not always present. In fact, other sources can induce torsion as the default of symmetry of the muscle axis, which we will discuss later. In Fig.6(F)-(G), we demonstrate that the curvature provided by the model increases as muscle activation increases and that the torsion is not simply related to the activation amplitude since it also depends on the value of the angle $\alpha_a$, reaching a maximum at approximately

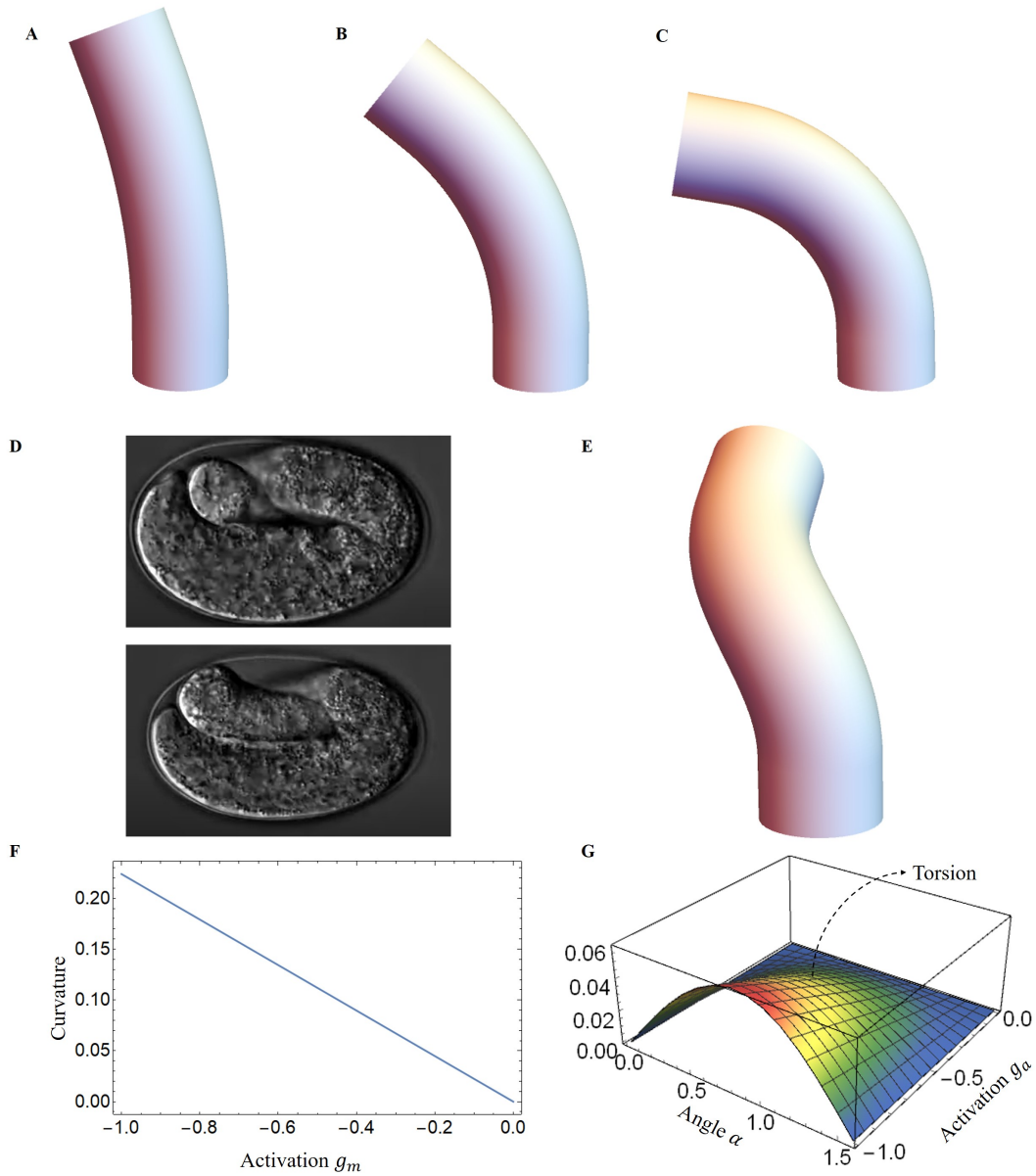


**Figure 6.** Deformed configurations for different activation for muscles, (A) $g_m = -0.02, \alpha_a = \pi/3, g_a = -0.01$. (B) $g_m = -0.05,\ \alpha_a = \pi/4,\ g_a = -0.01$. (C) $g_m = -0.08,\ \alpha_a = \pi/6,\ g_a = -0.01$. (D) The graphs were captured from the Hymanlab, and the website: https://www.youtube.com/watch?v=M2ApXHhYbaw. The movie was acquired at a temperature of $20^0C$ using DIC optics. (E) $g_m = -0.1,\ \alpha_a = \pi/4,\ g_a = -0.7$. (F) Curvature is plotted as a function of muscle activation. (G) Torsion is plotted as a function of the actin activation and angle of actin fibers.

$\pi/4$. Detailed calculations are shown in Section Methods and Materials and Appendix 4.

## Energy transformation and Elongation

During the late elongation process, the four internal muscle bands cyclically contract in pairs (***Yang (2017)***; ***Williams and Waterston (1994)***). Each contraction of a pair increases the energy of the system under investigation, which is then rapidly released to the body. This energy exchange causes the torsion-bending energy to convert into elongation energy, leading to a length increase during the relaxation phase, as shown in Fig.1 of the Appendix 5. With all deformations obtained, Eq.(2) can be used to calculate the accumulated energy $W_c$ produced by both the muscles and the acto-myosin activities during a contraction. Subsequently, when the muscles on one side relax,

the worm body reverts to its original shape but with a tiny elongation corresponding to the transferred elastic energy. This new state involves the actin network adopting a 'loop' configuration with a strain of $\varepsilon g_{a1}$ once relaxation is complete. If all accumulated energy from the bending-torsion deformation goes towards elongating the worm body, the accumulated energy $W_c$ and energy $W_r$ following muscle relaxation are equivalent. The activation of actin fibers $g_{a1}$ after muscle relaxation can be calculated and determined by our model.

Once the first stage is well characterized, we can quantify the total energy resulting from both muscles and acto-myosin after each contraction. Then, we used our model to predict elongation in the wild-type *C. elegans*, unc-112(RNAi) mutant and spc-1(RNAi) pak-1(tm403) mutant and further compared the results with experimental observations. The length of the wild type elongates from approximately $90\ \mu m$ to $210\ \mu m$ during the muscle-activated phase (***Lardennois et al.*** (***2019***)), the phase lasts about $140$ minutes, and the average time interval between two contractions is about $40$ seconds (***Yang*** (***2017***)), so the number of contractions can be estimated to be around $210$ times. Unfortunately, due to the difficulty to realize quantitative experiments on an embryo always in agitation in the egg shell between bending, torsion, and also rotations around its central axis, one can hypothesize several scenarios: at each step $i$ between state $A_{i,0}$ to $A_{i,1}$ and then $A_{i,2}$, the whole mechanical muscle-myosin energy is transferred to the elongated step $A_{i,2}$, leading to a small $\delta\zeta_i$.

Considering the experimental results shown in Fig.7(B), we determine the optimal values for the activation parameters: $g_m = -0.15$ and $g_a = -0.01$ assuming that all the accumulated energy during muscle activation is transferred to elongation($W_r = W_c$). The elementary elongation $\delta\zeta_i$ will be gradually increased with time, which is shown as the black line in Fig.7(A). At the beginning, $\delta\zeta_i$ is about $0.5\mu m$, but at the end of this process, $\delta\zeta_i$ is about $1.5\mu m$, indicating that the worm will elongate up to $290\mu m$. The result is significantly higher than our actual size $210\mu m$. When the elongation proceeds, we assume a transfer of energy between bending-torsion-contraction and elongation but it may be not fully effective, which means a significant part of the energy is lost. From the experimental data, we evaluate that the energy loss gradually increases, from full conversion at the beginning to only $40\%$ of the accumulated energy used for elongation at the end of the process ($W_r = 0.4W_c$). It induces for $\delta\zeta_i$ a first increase and then a decrease, which is shown as the blue line in Fig.7(A) and is responsible for the slowdown around $200$ mins. This option, which may be not the only possible one, leads to the estimated elongation having a good agreement with experimental data (see the blue-dashed curve in Fig.7(B)). Indeed it is possible that the *C. elegans* elongation requires other transformations which will cost energy. As the embryo gradually elongates, energy dissipation and the biomechanical energy required to reorganize the actin bundles may be two factors that contribute to the increased energy loss that underlies the hypothesis.

Moreover, it was reported in (***Norman and Moerman*** (***2002***)) that the knockdown of unc-112(RNAi), known for impairing muscle contractions, results in the arrest of elongation of embryos at the twofold stage, indicating that muscles have no activation, $g_m = 0$ in our model, and no accumulated energy can be converted into elongation. Another mutation concerning the embryos consisting of mutant cells with pak-1(tm403), known to regulate the activity of myosin motors leads to a retraction of the embryo, so the pre-stretch caused by myosin will not be maintained and will decrease. These aforementioned findings are fully consistent with a variety of experimental observations and are shown in Fig.7(B).

## Embryo rotations and dissipation

The main manifestation of the muscle activity, independently of the elongation, is probably the constant rotations of the embryo despite its confinement in the egg. This can be explained by a small angular deviation of the muscle sarcomeres from the central axis due to their attachment to the inner boundary of the cell epidermis, the so-called "dense bodies" (***Moerman and Williams*** (***2006***)). Since they cross the horizontal plane at approximately $\pm 45°$ and the deviation $\beta_m$ from the anterior-posterior axis is estimated to be about $6°$ each active muscle on the left (or on the right) contributes to the torque via a geometrical factor about $a_g = \sin(6\pi/180)\cos(\pi/4)$. Then a simple

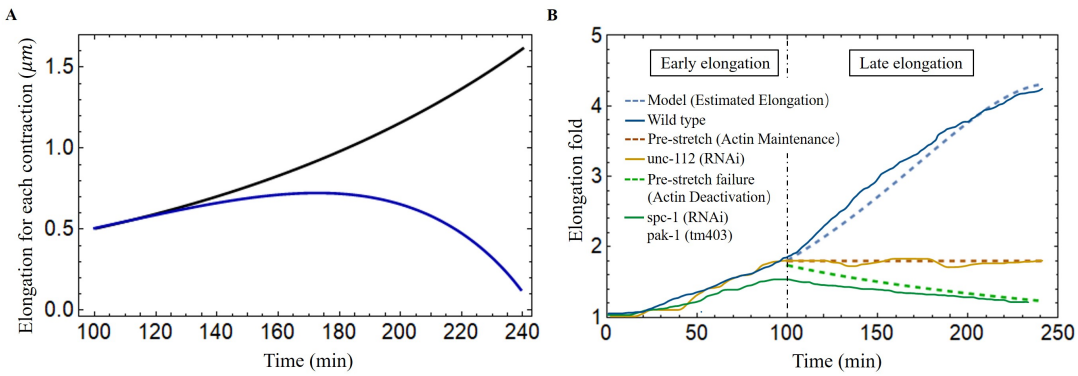


**Figure 7.** (A) The elongation for each contraction varies with time. Black line: all energy converted to the elongation, blue line: partial energy converted to the elongation. The activation: $g_m = -0.15$, $g_a = -0.01$. (B) The model predicted results agree well with the experimental data of wild-type and different mutant *C. elegans* embryos (***Lardennois et al.*** (***2019***)). The activation of wild type model (blue dashed line): $g_m = -0.15$, $g_a = -0.01$. The activation of unc-112(RNAi) (brown dashed line): $g_m = 0$, $g_a = 0$. In the pre-stretch failure case (green dashed line), $\lambda$ will decrease from $1.8$.

estimation of the muscle activity in terms of torque reads $\Lambda_m \sim \mu_m \pi R^3 s_m p_m a_g(\epsilon g_m)$ where $s_m$ is the surface of the muscle pair on the left (or right) compared to the section of the cylinder: $s_m = 0.025$ and $p_m$ is the distance of the muscles from the central axis of the embryo: $p_m = 0.75$ while $g_m = 0.15$ according to the analysis of the elongation. So the muscles on one side contribute to a torque $\Lambda_m$ along the axis of symmetry given by $\Lambda_m = 4.657\mu_m \pi R^3 \cdot 10^{-5}$.

Let us consider now the dissipative torque, assuming that the dynamics of rotation is stopped by friction after one bending event. Two cases can be considered: either the dissipation comes from viscous flow or from the rubbing of the embryo when it folds. The fluid dissipation results from the rotations in the interstitial fluid inside and along the egg shell since the anterior-posterior axis remains parallel to the egg-shell (***Bhatnagar et al.*** (***2023***)) The interstitial fluid, of viscosity $\eta$ contains a significant amount of sugar and other molecules which are required for embryo survival and then is more viscous than water (***Labouesse*** (***2023***)). However, values for sucrose or sorbitol at the concentration of $1$ mole/liter indicates a viscosity of order a few times the viscosity of water, which is $1$ mPas. For example at $0.9$ mole/liter and temperature of $20°$, an aqueous solution with sorbitol has a viscosity of $1.6$ mPas, which can be extrapolated to $\eta = 1.9$ mPas at $1.2$ mole/liter (***Jiang et al.*** (***2013***)). The estimation given by an embryo located in the middle of the egg-shell, gives a weaker viscous torque once evaluated by $\Lambda_v = 4\pi\eta\Omega_e L R^2 \left(R_{egg}^2/(R_{egg}^2 - R^2)\right)$ according to a classical result reported by Landau *et al.* (***Landau and Lifshitz*** (***1971***, 2013)). It has to be mentioned that this estimation assumes that the two cylinders: the egg shell and the embryo have the same axis of symmetry and concerns the beginning of the muscle activity where the radius is about $8.2\ \mu m$, the length is $90\ \mu m$,the radius of the shell about $R_{egg} = 15\mu m$ and the length $L_{egg} = 54\mu m$, see Fig.6(D). The angular velocity $\Omega_e$ is more difficult to evaluate but it is about $90°$ per two seconds deduced from videos. When the embryo approaches the egg shell, the friction increases, and two eccentric cylinders of different radii have to be considered with the two axes of symmetry separated by a distance $d$. The hydrodynamic study in this case is far from being trivial, and seems to have been initiated first by Zhukoski (***Zhukoski*** (***1887***)) who suggested the use of bipolar coordinates for the mathematical treatment. Many following contributions established with different simplified assumptions have been published after and the study was fully revisited by Ballal and Rivlin (***Ballal and Rivlin*** (***1976***)). Here we focus on the limit of a small gap $\delta$ between the rotating body-shape and the egg and by considering an asymptotic analysis at small $\delta$ of the general result derived in (***Ballal and Rivlin*** (***1976***)). Thus, the viscous torque reads $\tilde{\Lambda}_v = 2\sqrt{2}\pi\eta\Omega_e L_c R_{egg}^2 \sqrt{R_{egg}/\delta}\sqrt{(R_{egg} - d)/d}$. $L_c$ is the zone of contact with the egg and $d = R_{egg} - \delta - R$. This approach is an approximation since the

embryo has more of a torus shape than a cylinder (***Yang Xinyi et al.*** (***2023***)) but the evaluation of the dissipation is satisfactory for $\delta = 0.5\mu m, \Omega_e \sim \pi/4\, s^{-1}$ and $\mu = 10^5 Pa$. Coming back to the first model of dissipation with the same data, the ratio between the dissipative viscous torque and the active one gives: $\Lambda_v/\Lambda_m = 0.02$, which is obviously unsatisfactory. Finally, the dissipative energy $\mathcal{E}_{diss}$ during one bending event leading to an angle of $\pi/2$ is $\mathcal{E}_{diss} = 1/2\Lambda_m \times (\pi/2)^2$ which represents $4\%$ of the muscle elastic energy during the bending so at the beginning of the muscle activity (Appendix 5, Eq.(45)), the dissipation exits but is negligible. At the very end of the process, this ratio becomes $60\%$ but as yet mentioned our estimation for the dissipation becomes very approximate, increases a lot due to the embryo confinement, and does not involve the numerous biochemistry steps necessary to reorganize the active network: acto-myosin and muscles.

## Discussion

Since the discovery of the muscle activity before the egg hatch of the *C. elegans* embryo, it has become critical to explain the role of mechanical forces generated by muscle contraction on the behavioral and functional aspects of the epidermis. We provide a mechanical model in which the *C. elegans* is simplified as a cylinder, and the muscle bands and actin that drive its elongation are modeled as active structures in a realistic position. We determine the fiber orientation using experimental observations and then calculate the deformation by tensorial analysis involving the strains generated by the active components. Although a special focus is made on late elongation, its quantitative treatment cannot avoid the influence of the first stage of elongation due to the acto-myosin network, which is responsible for a pre-strain of the embryo. In a finite elasticity formalism, the deformations induced by muscles in a second step are coupled to the level of strains of the initial elongation period. For that, we need to revisit the theory of the acto-myosin contraction and previous results (***Ciarletta et al.*** (***2009***); ***Vuong-Brender et al.*** (***2017a***); ***Ben Amar et al.*** (***2018***)) to unify the full treatment. In particular, a model for the recruitment of active myosin motors under forcing is presented which recovers the experimental results of the first elongation stage.

The elongation process of *C. elegans* during the late period is much more complex than the early elongation stage which is caused only by actin contraction. During the late elongation, the worm is distorted by the combined action of muscle and acto-myosin, resulting in an energy-accumulating process. Bending deformation is a phenomenon resulting from unilateral muscular contraction, and during the late elongation, significant torsional deformation is observed, indicating that the bending process induces a reorientation of the actin fibers. It is worth noting that the embryo is always rotating in tandem with the muscle activity making difficult any experimental measurements. However, our model can predict that if the muscles are not perfectly vertical, torque exits that causes rotation and eventually torsion. The accumulated energy is then partly turned into energy for the ongoing action of actin, allowing the embryo to elongate when the muscle relaxes. Both sides of the *C. elegans* muscles contract in a sequential cycle, repeating the energy conversion process, and eventually completing the elongation process. However, the energy exchange between bending and elongation is limited, among other factors, by the viscous dissipation induced by rotation, which is also evaluated in this study. Not investigated in detail here is the necessary re-organization of the active networks (acto-myosin and muscles) due to this tremendous shape transformation of the embryo. In parallel to elongation, the cuticle is built around the body (***Page and Johnstone*** (***2007***)). This very thin and stiff membrane ensures protection and locomotion post-hatching. Clearly, these processes will perturb muscle activity. These two aspects which intervene in the final stage of the worm confinement play a very important role at the frontier across scales between genetics, biochemistry and mechanics.

Finally, the framework presented here not only provides a theoretical explanation for embryonic elongation in *C. elegans*, it can also be used to model other biological behaviors, such as plant tropism (***Moulton et al.*** (***2020b***)) and elephant trunk elongated (***Schulz et al.*** (***2022b***,*a*)) and bending. Our ideas could potentially be used in the emerging field of soft robotics, like octopus legs-inspired robots (***Kang et al.*** (***2012***); ***Nakajima et al.*** (***2013***); ***Calisti et al.*** (***2015***)), which is soft and its deforma-

tion induced by muscles activation. We can reliably predict deformation by knowing the position of activation and the magnitude of forces in the model. Furthermore, residual stresses can be incorporated into our model to fulfill design objectives.

## Methods and Materials

The model has been presented in a series of articles by A. Goriely and collaborators (***Goriely and Tabor*** (***2013***); ***Moulton et al.*** (***2013***, 2020b); ***Kaczmarski et al.*** (***2022***); ***Goriely et al.*** (***2022***)). As one imagines, it is far from triviality and most of the literature on this subject concerns either full cylinders or cylindrical shells in torsion around the axis of symmetry, the case of bending is more overlooked. However, the geometry of the muscles in *C. elegans* leads automatically to a bending process that cannot be discarded. We take advantage of these previous works and apply the methodology to our model.

### The deformation gradient

The axial extension $\zeta$ is obtained by $\mathbf{r}'(Z) = \zeta \mathbf{d}_3$, where $'$ denotes the first derivative with respect to the material coordinate $Z$. From the director basis, the Darboux curvature vector reads: $\mathbf{u} = u_1\mathbf{d}_1 + u_2\mathbf{d}_2 + u_3\mathbf{d}_3$, this vector gives the evolution of the director basis along the filamentary line as: $\mathbf{d}_i{}'(Z) = \zeta \mathbf{u} \times \mathbf{d}_i$, see Fig.3(A).

The finite strain $\mathbf{G}_0$ can map the initial stress-free state $\mathcal{B}_0$ to a state $\mathcal{B}_1$, which reflects early elongation process. After in the residually stressed $\mathcal{B}_1$, we impose an incremental strain field $\mathbf{G}_1$ maps the body to $\mathcal{B}_2$, which represents late elongation process. So, the deformation gradient can be expressed as: $\mathbf{F} = \mathbf{F}_e\mathbf{G}_1\mathbf{G}_0$ (***Goriely and Ben Amar*** (***2007***)). The deformation gradient $\mathbf{F} = F_{ij}\mathbf{d}_i \otimes \mathbf{e}_j,\ i \in \{1,2,3\}$ and $j$ labels the reference coordinates $\{R, \Theta, Z\}$ finally reads:

$$\mathbf{F} = \begin{bmatrix} a_{1R} & \frac{1}{R}a_{1\Theta} & \lambda\varepsilon\,(1+\varepsilon\xi)\left(u_2a_3 - u_3a_1\sin a_2\right) \\ a_1a_{2R} & \frac{a_1}{R}a_{2\Theta} & \lambda\varepsilon\,(1+\varepsilon\xi)\left(u_3a_1\cos a_2 - u_1a_3\right) \\ a_{3R} & \frac{1}{R}a_{3\Theta} & \lambda\,(1+\varepsilon\xi)\left(1+\varepsilon\left(u_1a_1\sin a_2 - u_2a_1\cos a_2\right)\right) \end{bmatrix}, \tag{4}$$

where $\lambda$ is the axial extension due to the pre-strained.

We define $\mathbf{G}_0 = Diag\,(1, 1+\varepsilon c, 1)$, since $g_0 = 0.88$ can be determined through the early elongation, we write it in the form of $1+\varepsilon c$ to simplify the calculation, $c \approx -0.6$ ($\varepsilon \approx 0.2$).

Let us consider fibers oriented along the unit vector $\mathbf{m} = (\sin\alpha\sin\beta, \sin\alpha\cos\beta, \cos\alpha)$ for the incremental strain $\mathbf{G_1}$, where $\alpha$ and $\beta$ characterise the angles with $\mathbf{e_z}$ and $\mathbf{e}_\theta$ and can be found in Fig.3(A). The active filamentary tensor in cylindrical coordinates is then $\mathbf{G} = \mathbf{G}_0\,(\mathbf{I} + \varepsilon g\ \mathbf{m}\otimes\mathbf{m})$, see (***Holzapfel*** (***2002***)) which reads:

$$\mathbf{G} = \mathbf{G_0} + \varepsilon g \mathbf{G_0} \begin{bmatrix} \sin^2\alpha\sin^2\beta & \sin^2\alpha\sin\beta\cos\beta & \sin\alpha\cos\alpha\sin\beta \\ \sin^2\alpha\sin\beta\cos\beta & \sin^2\alpha\cos^2\beta & \sin\alpha\cos\alpha\cos\beta \\ \sin\alpha\cos\alpha\sin\beta & \sin\alpha\cos\alpha\cos\beta & \cos^2\alpha \end{bmatrix}. \tag{5}$$

### The energy function

The auxiliary strain-energy density can be obtained by expanding the inner variables $a_i$ (see Eq.(1)), $p_i$ and the potential $V$ (see Eq.(2)) as:

$$\mathbf{a} = \mathbf{a}^{(0)} + \varepsilon\mathbf{a}^{(1)} + \varepsilon^2\mathbf{a}^{(2)} + \mathcal{O}\left(\varepsilon^3\right), \tag{6}$$

$$p = p^{(0)} + \varepsilon p^{(1)} + \varepsilon^2 p^{(2)} + O\left(\varepsilon^3\right), \tag{7}$$

$$V(\mathbf{F}_e, \mathbf{G}) = V_0 + \varepsilon V_1 + \varepsilon^2 V_2 + O\left(\varepsilon^3\right). \tag{8}$$

For each cross-section, the associated Euler-Lagrange equations take the following form:

$$\frac{\partial}{\partial R}\frac{\partial V_iR}{\partial a_{jR}^{(k)}} + \frac{1}{R}\frac{\partial V_iR}{\partial a_{jR}^{(k)}} + \frac{\partial}{\partial\Theta}\frac{\partial V_iR}{\partial a_{j\Theta}^{(k)}} - \frac{\partial V_iR}{\partial a_j^{(k)}} = 0, \tag{9}$$

where $j = 1, 2, 3, k = 0, 1$, in association with boundary conditions at each order $k = 0, 1$ on the outer radius $R_i$:

$$\left.\frac{\partial V_i R}{\partial a_{jR}^{(k)}}\right|_{R=R_i} = 0, j = 1, 2, 3. \tag{10}$$

We solve these equations order by order and consider incompressibility. At the lowest order, the incompressibility imposes the deformation: $\mathbf{a}^{(0)} = (r(R), \Theta, 0)$ and the Euler-Lagrange equation gives the Lagrange parameter $p^{(0)} = P_0(R)$ which finally read:

$$r' = \frac{R}{\lambda r},\ P_0{}' = 0, \tag{11}$$

and the boundary condition $\sigma_{rr}(R = 1) = 0$ gives the value of $P_0 = 1/\lambda$. At $\mathcal{O}(\varepsilon)$, the Euler-Lagrange equations are again automatically satisfied, and at $\mathcal{O}\left(\varepsilon^2\right)$, the crucial question is to get the correct expression for $a_i^{(1)}$ and $p^{(1)}$. Based on the previous subsection, the following form is intuited:

$$\begin{aligned}
a_1^{(1)} &= -\frac{1}{2} r(R)\,\xi + q_1 r(R)^2 \left(u_1 \sin\Theta - u_2 \cos\Theta\right) + h_1(R) \\
a_2^{(1)} &= q_2 r(R) \left(u_1 \cos\Theta + u_2 \sin\Theta\right) + h_2(R) \\
a_3^{(1)} &= \lambda\xi \\
p^{(1)} &= h_3(R)
\end{aligned} \tag{12}$$

As before, the Euler-Lagrange equations and incompressibility condition give the two constants $q_1 = \frac{1}{8}\left(-2 + \lambda^3\right)$, $q_2 = \frac{1}{8}\left(2 + 3\lambda^3\right)$ and $h_1$, $h_2$, $h_3$ are a function of $R$. With the solutions for active strain $\mathbf{a}^{(0)}$ and $\mathbf{a}^{(1)}$, full expressions of them are given in the Appendix 4. The second order energy takes the form:

$$\mathcal{E} = \varepsilon^4 \int_0^L \mathrm{d}Z \int_S V_2\left(\mathbf{a}^{(0)}, \mathbf{a}^{(1)}; \mathrm{u}_1, \mathrm{u}_2, \mathrm{u}_3, \xi\right) R\mathrm{d}R\ \mathrm{d}\Theta + \mathcal{O}\left(\varepsilon^5\right), \tag{13}$$

and we can transform it into this form:

$$V_2 R = A_1\xi + A_2\xi^2 + B_1 u_1 + B_2 {u_1}^2 + C_1 u_2 + C_2 {u_2}^2 + D_1 u_3 + D_2 {u_3}^2, \tag{14}$$

where $A_i$, $B_i$, $C_i$ and $D_i$ are functions of $R$ and $\Theta$.

## The method for determining deformation

Comparing with the energy of an extensible elastic rod (***Moulton et al.*** (***2020a***); ***Kirchhoff and Hensel*** (***1883***); ***Mielke*** (***1988***); ***Mora and Müller*** (***2002***, 2004)), we recognize the classic extensional stiffness $K_0$, bending stiffness $K_1$ and $K_2$, torsional stiffness $K_3$ coefficients:

$$K_0 = \int_{S_K} A_2 d\,R d\Theta,\ K_1 = \int_{S_K} B_2 d\,R d\Theta,\ K_2 = \int_{S_K} C_2 d\,R d\Theta,\ K_3 = \int_{S_K} D_2 d\,R d\Theta, \tag{15}$$

where $A_2$, $B_2$, $C_2$ and $D_2$ are related to the shear modulus $\mu$, so for a uniform material with no variations of shear modulus, $S_K$ represents the cross-section of the cylinder. But if not, we need to divide different regions to perform the integration.

We now focus on the intrinsic extension and curvatures of the cylindrical object induced by the active strains, this requires the competition of the active forces with the stiffness of the cylindrical bar following the relationships,

$$\hat{\zeta} = 1 - H_0/K_0,\ \hat{u}_1 = -H_1/K_1, \hat{u}_2 = H_2/K_2,\ \hat{u}_3 = -H_3/K_3, \tag{16}$$

where $H_i$ calculated by:

$$H_0 = \frac{1}{2}\int_{S_H} A_1 d\,R d\Theta,\ H_1 = \frac{1}{2}\int_{S_H} B_1 d\,R d\Theta,\ H_2 = \frac{1}{2}\int_{S_H} C_1 d\,R d\Theta,\ H_3 = \frac{1}{2}\int_{S_H} D_1 d\,R d\Theta. \tag{17}$$

where $A_1$, $B_1$, $C_1$ and $D_1$ are related to the shear modulus $\mu$,the fiber angles $\alpha$ and $\beta$, and the activation $g$. So, the integration region $S_H$ is divided into the different parts of the embryo which all contribute to the deformation.

To calculate the intrinsic Frenet curvature and torsion, we use the following equation:

$$\hat{\kappa} = \sqrt{\hat{u}_1^2 + \hat{u}_2^2} \quad \text{and} \quad \hat{\tau} = \frac{\hat{u}_3}{\hat{\zeta}}. \tag{18}$$

Finally, for the case of activated left side muscles, we can calculate intrinsic extension and curvatures by Eq.16), $\hat{u}_{1m} = 0$ and $\hat{u}_{3m} = 0$, so the intrinsic Frenet curvature and torsion Eq.(18), $\hat{\kappa}_m = \hat{u}_{2m}$ and $\hat{\tau}_m = 0$. For the activated actin case, we can calculate intrinsic extension and curvatures by Eq.(16), $\hat{u}_{1a} = 0$ and $\hat{u}_{2a} = 0$, and the intrinsic Frenet curvature and torsion Eq.(18), $\hat{\kappa}_a = 0$ and $\hat{\tau}_a = \frac{\hat{u}_{3a}}{\hat{\zeta}_a}$. These quantities have been used to calculate the deformation images, as shown previously in Fig.6.

After obtaining all solutions, we can use these quantities to calculate the accumulated energy $W_c$ in the system after one contraction by Eq.(2). By defining the activation ($g_m$ and $g_a$) and the conversion efficiency of energy, we can obtain the activation ($g_{a1}$) of the actin bundles after once contraction and further calculate the elongation.

All calculation results and parameters are presented in the Appendix.

## Acknowledgments

It is a pleasure to acknowledge fruitful discussions with Michel Labouesse and Kelly Molnar about experimental observations concerning the embryonic *C.elegans* elongation. We also thank Alain Goriely for his help with the technical aspects of nonlinear elasticity. Both authors acknowledge the support of the contract EpiMorph (ANR-2018-CE13-0008). Anna Dai acknowledges the support of the CSC (China Scholarship Council), file No. 201906250173.

## References

**Ballal B**, Rivlin R. Flow of a Newtonian fluid between eccentric rotating cylinders: inertial effects. Archive for Rational Mechanics and Analysis. 1976; 62:237–294.

**Ben Amar M**, Bordner A. Mimicking cortex convolutions through the wrinkling of growing soft bilayers. Journal of Elasticity. 2017; 129(1):213–238.

**Ben Amar M**, Jia F. Anisotropic growth shapes intestinal tissues during embryogenesis. Proceedings of the National Academy of Sciences. 2013; 110(26):10525–10530.

**Ben Amar M**, Qiuyang-Qu P, Vuong-Brender TTK, Labouesse M. Assessing the contribution of active and passive stresses in C. elegans elongation. Physical Review Letters. 2018; 121(26):268102.

**Bertet C**, Sulak L, Lecuit T. Myosin-dependent junction remodelling controls planar cell intercalation and axis elongation. Nature. 2004; 429(6992):667–671.

**Bhatnagar A**, Nestler M, Gross P, Kramar M, Leaver M, Voigt A, Grill SW. Axis convergence in C. elegans embryos. bioRxiv. 2023; p. 2023–03.

**Blankenship JT**, Backovic ST, Sanny JS, Weitz O, Zallen JA. Multicellular rosette formation links planar cell polarity to tissue morphogenesis. Developmental cell. 2006; 11(4):459–470.

**Bouchard A**, Hofland GW, Witkamp GJ. Properties of sugar, polyol, and polysaccharide water- ethanol solutions. Journal of Chemical & Engineering Data. 2007; 52(5):1838–1842.

**Calisti M**, Corucci F, Arienti A, Laschi C. Dynamics of underwater legged locomotion: modeling and experiments on an octopus-inspired robot. Bioinspiration & biomimetics. 2015; 10(4):046012.

**Chadwick R**. Slow viscous flow inside a torus—the resistance of small tortuous blood vessels. Quarterly of applied mathematics. 1985; 43(3):317–323.

**Ciarletta P**, Ben Amar M, Labouesse M. Continuum model of epithelial morphogenesis during Caenorhabditis elegans embryonic elongation. Philosophical Transactions of the Royal Society A: Mathematical, Physical and Engineering Sciences. 2009; 367(1902):3379–3400.

**Ciarletta P**, Ben Amar M. Papillary networks in the dermal–epidermal junction of skin: a biomechanical model. Mechanics Research Communications. 2012; 42:68–76.

**Coulombre AJ**, Coulombre JL. Intestinal development: I. Morphogenesis of the villi and musculature. Journal of Embryology and Experimental Morphology. 1958; 6(3):403–411.

**Cowan CR**, Hyman AA. Acto-myosin reorganization and PAR polarity in C. elegans. Development. 2007; 134(6):1035–1043.

**De Vita R**, Grange R, Nardinocchi P, Teresi L. Mathematical model for isometric and isotonic muscle contractions. Journal of Theoretical Biology. 2017; 425:1–10.

**Denham JE**, Ranner T, Cohen N. Signatures of proprioceptive control in Caenorhabditis elegans locomotion. Philosophical Transactions of the Royal Society B: Biological Sciences. 2018; 373(1758):20180208.

**Gally C**, Wissler F, Zahreddine H, Quintin S, Landmann F, Labouesse M. Myosin II regulation during C. elegans embryonic elongation: LET-502/ROCK, MRCK-1 and PAK-1, three kinases with different roles. Development. 2009; 136(18):3109–3119.

**Goriely A**. The mathematics and mechanics of biological growth, vol. 45. Springer; 2017.

**Goriely A**, Ben Amar M. On the definition and modeling of incremental, cumulative, and continuous growth laws in morphoelasticity. Biomechanics and modeling in mechanobiology. 2007; 6(5):289–296.

**Goriely A**, Geers MG, Holzapfel GA, Jayamohan J, Jérusalem A, Sivaloganathan S, Squier W, van Dommelen JA, Waters S, Kuhl E. Mechanics of the brain: perspectives, challenges, and opportunities. Biomechanics and modeling in mechanobiology. 2015; 14(5):931–965.

**Goriely A**, Moulton DE, Angela Mihai L. A rod theory for liquid crystalline elastomers. Journal of Elasticity. 2022; p. 1–24.

**Goriely A**, Tabor M. Rotation, inversion and perversion in anisotropic elastic cylindrical tubes and membranes. Proceedings of the Royal Society A: Mathematical, Physical and Engineering Sciences. 2013; 469(2153):20130011.

**Hannezo E**, Prost J, Joanny JF. Instabilities of monolayered epithelia: shape and structure of villi and crypts. Physical Review Letters. 2011; 107(7):078104.

**Hidayanto E**, Tanabe T, Kawai J. Measurement of viscosity and sucrose concentration in aqueous solution using portable Brix meter. Berkala Fisika. 2010; 13(2):23–28.

**Holzapfel GA**, Nonlinear solid mechanics: a continuum approach for engineering science. Kluwer Academic Publishers Dordrecht; 2002.

**Howard J**, Clark R. Mechanics of motor proteins and the cytoskeleton. Appl Mech Rev. 2002; 55(2):B39–B39.

**Jiang X**, Zhu C, Ma Y. Density and viscosity of sorbitol/maltitol in L-ascorbic acid aqueous solutions at T=(293.15 to 323.15) K. Journal of Molecular Liquids. 2013; 188:67–73.

**Kaczmarski B**, Moulton DE, Kuhl E, Goriely A. Active filaments I: Curvature and torsion generation. Journal of the Mechanics and Physics of Solids. 2022; 164:104918.

**Kang R**, Branson DT, Guglielmino E, Caldwell DG. Dynamic modeling and control of an octopus inspired multiple continuum arm robot. Computers & Mathematics with Applications. 2012; 64(5):1004–1016.

**Kirchhoff G**, Hensel K. Vorlesungen über mathematische Physik, vol. 1. Druck und Verlag von BG Teubner; 1883.

**Kücken M**, Newell AC. Fingerprint formation. Journal of theoretical biology. 2005; 235(1):71–83.

**Labouesse M**. Viscosity of the intersticial fluid. The fluid contained in the embryo egg is a highly viscous solution full of diverse sugars and other molecules necessary for metabolism The proof is given by the necessity to put the embryo in a solution when the hatching is achieved on purpose The survival of the embryo lasts few hours The solution is a sorbitol aqueous solution containing approximately 1-12 mole/L. 2023; .

**Landau L**, Lifshitz E. Mécanique des fluides, editions Mir, vol. 6; 1971.

**Landau LD**, Lifshitz EM. Fluid Mechanics: Landau and Lifshitz: Course of Theoretical Physics, Volume 6, vol. 6. Elsevier; 2013.

**Lardennois A**, Pásti G, Ferraro T, Llense F, Mahou P, Pontabry J, Rodriguez D, Kim S, Ono S, Beaurepaire E, et al. An actin-based viscoplastic lock ensures progressive body-axis elongation. Nature. 2019; 573(7773):266–270.

**Lesanpezeshki L**, Qadota H, Darabad MN, Kashyap K, Lacerda CM, Szewczyk NJ, Benian GM, Vanapalli SA. Investigating the correlation of muscle function tests and sarcomere organization in C. elegans. Skeletal muscle. 2021; 11(1):1–15.

**Levayer R**, Lecuit T. Biomechanical regulation of contractility: spatial control and dynamics. Trends in cell biology. 2012; 22(2):61–81.

**Li B**, Cao YP, Feng XQ, Gao H. Surface wrinkling of mucosa induced by volumetric growth: theory, simulation and experiment. Journal of the Mechanics and Physics of Solids. 2011; 59(4):758–774.

**Lv C**, Yang Y, Li B. Nano/micromotors in active matter. Micromachines. 2022; 13(2):307.

**McKeown C**, Praitis V, Austin J. sma-1 encodes a betaH-spectrin homolog required for Caenorhabditis elegans morphogenesis. Development. 1998; 125(11):2087–2098.

**Mielke A**. On Saint-Venant's problem for an elastic strip. Proceedings of the Royal Society of Edinburgh Section A: Mathematics. 1988; 110(1-2):161–181.

**Moerman DG**, Williams BD. Sarcomere assembly in *C. elegans* muscle. WormBook: The Online Review of C elegans Biology [Internet]. 2006; .

**Mora MG**, Müller S. Derivation of the nonlinear bending-torsion theory for inextensible rods by Gamma-convergence. preprint. 2002; .

**Mora MG**, Müller S. A nonlinear model for inextensible rods as a low energy $\Gamma$-limit of three-dimensional nonlinear elasticity. Annales de l'Institut Henri Poincaré C. 2004; 21(3):271–293.

**Moulton D**, Lessinnes T, Goriely A. Morphoelastic rods. Part I: A single growing elastic rod. Journal of the Mechanics and Physics of Solids. 2013; 61(2):398–427.

**Moulton DE**, Lessinnes T, Goriely A. Morphoelastic rods III: Differential growth and curvature generation in elastic filaments. Journal of the Mechanics and Physics of Solids. 2020; 142:104022.

**Moulton DE**, Oliveri H, Goriely A. Multiscale integration of environmental stimuli in plant tropism produces complex behaviors. Proceedings of the National Academy of Sciences. 2020; 117(51):32226–32237.

**Nakajima K**, Hauser H, Kang R, Guglielmino E, Caldwell DG, Pfeifer R. A soft body as a reservoir: case studies in a dynamic model of octopus-inspired soft robotic arm. Frontiers in computational neuroscience. 2013; 7:91.

**Nardinocchi P**, Teresi L. On the active response of soft living tissues. Journal of Elasticity. 2007; 88(1):27–39.

**Norman KR**, Moerman DG. $\alpha$ spectrin is essential for morphogenesis and body wall muscle formation in Caenorhabditis elegans. The Journal of cell biology. 2002; 157(4):665–677.

**Olson MF**, Sahai E. The actin cytoskeleton in cancer cell motility. Clinical & experimental metastasis. 2009; 26(4):273–287.

**Page AP**, Johnstone I. The cuticle. WormBook. 2007; .

**Palumbo S**, Benvenuti E, Fraldi M. Actomyosin contractility and buckling of microtubules in nucleation, growth and disassembling of focal adhesions. Biomechanics and Modeling in Mechanobiology. 2022; 21:1–14.

**Priess JR**, Hirsh DI. Caenorhabditis elegans morphogenesis: the role of the cytoskeleton in elongation of the embryo. Developmental biology. 1986; 117(1):156–173.

**Rodriguez EK**, Hoger A, McCulloch AD. Stress-dependent finite growth in soft elastic tissues. Journal of biomechanics. 1994; 27(4):455–467.

**Saxena A**, Denholm B, Bunt S, Bischoff M, VijayRaghavan K, Skaer H. Epidermal growth factor signalling controls myosin II planar polarity to orchestrate convergent extension movements during Drosophila tubulogenesis. PLoS biology. 2014; 12(12):e1002013.

**Schulz A**, Dimitriyev M, Singal K, Sordilla S, Sahin A, Boyle C, Higgins C, Matsumoto E, Hu D. Creating bio-inspired tissue mimics of African elephant trunks' wrinkled and folded skin. In: *APS March Meeting Abstracts*, vol. 2022; 2022. p. Z08–010.

**Schulz AK**, Boyle M, Boyle C, Sordilla S, Rincon C, Hooper S, Aubuchon C, Reidenberg JS, Higgins C, Hu DL. Skin wrinkles and folds enable asymmetric stretch in the elephant trunk. Proceedings of the National Academy of Sciences. 2022; 119(31):e2122563119.

**Serra M**, Nájera GS, Chuai M, Spandan V, Weijer CJ, Mahadevan L. A mechanochemical model recapitulates distinct vertebrate gastrulation modes. bioRxiv. 2021; p. 2021–10.

**Shindo A**, Wallingford JB. PCP and septins compartmentalize cortical actomyosin to direct collective cell movement. Science. 2014; 343(6171):649–652.

**Shyer AE**, Tallinen T, Nerurkar NL, Wei Z, Gil ES, Kaplan DL, Tabin CJ, Mahadevan L. Villification: how the gut gets its villi. Science. 2013; 342(6155):212–218.

**Soesanto T**, Williams MC. Volumetric interpretation of viscosity for concentrated and dilute sugar solutions. The journal of physical chemistry. 1981; 85(22):3338–3341.

**Sulston JE**, Schierenberg E, White JG, Thomson JN. The embryonic cell lineage of the nematode Caenorhabditis elegans. Developmental biology. 1983; 100(1):64–119.

**Tallinen T**, Chung JY, Rousseau F, Girard N, Lefèvre J, Mahadevan L. On the growth and form of cortical convolutions. Nature Physics. 2016; 12(6):588–593.

**Tan T**, De Vita R. A structural constitutive model for smooth muscle contraction in biological tissues. International Journal of Non-Linear Mechanics. 2015; 75:46–53.

**Telis VRN**, Telis-Romero J, Mazzotti H, Gabas AL. Viscosity of aqueous carbohydrate solutions at different temperatures and concentrations. International Journal of food properties. 2007; 10(1):185–195.

**Toro R**, Burnod Y. A morphogenetic model for the development of cortical convolutions. Cerebral cortex. 2005; 15(12):1900–1913.

**Vicente-Manzanares M**, Ma X, Adelstein RS, Horwitz AR. Non-muscle myosin II takes centre stage in cell adhesion and migration. Nature reviews Molecular cell biology. 2009; 10(11):778–790.

**Vuong-Brender TTK**, Ben Amar M, Pontabry J, Labouesse M. The interplay of stiffness and force anisotropies drives embryo elongation. Elife. 2017; 6:e23866.

**Vuong-Brender TTK**, Suman SK, Labouesse M. The apical ECM preserves embryonic integrity and distributes mechanical stress during morphogenesis. Development. 2017; 144(23):4336–4349.

**Williams BD**, Waterston RH. Genes critical for muscle development and function in Caenorhabditis elegans identified through lethal mutations. The Journal of cell biology. 1994; 124(4):475–490.

**Yang X**. Remodelage des jonctions sous stress mécanique. PhD thesis, Université de Strasbourg; 2017.

**Yang Xinyi FT**, Kelly Molnar NM, Loic Royer JP, Stephan Grill GM, Labouesse M. Planar asymmetry in epithelial junction elongation results from repeated muscle contraction events. Preprint Sorbonne University. 2023; .

**Zhang H**, Landmann F, Zahreddine H, Rodriguez D, Koch M, Labouesse M. A tension-induced mechanotransduction pathway promotes epithelial morphogenesis. Nature. 2011; 471(7336):99–103.

**Zhukoski NE**. Conference. Comm Math Soc Kharkov. 1887; 17:31–46.

# Appendix 1

## Size and material parameters

**Appendix 1—table 1.** Parameters adopted in this work

| | | | | | |
|---|---|---|---|---|---|
| Geometry parameters | Normalized radius[1] | $R_1$=0.7 | $R_2$=0.8 | $R_2'$=0.96 | $R_3$=1 |
| | The location of muscles[2] | $\theta_1 = \frac{2}{3}\pi$<br>$\theta_2 = \frac{5}{6}\pi$ | $\theta_3 = \frac{7}{6}\pi$<br>$\theta_4 = \frac{4}{3}\pi$ | $\theta_5 = \frac{5}{3}\pi$<br>$\theta_6 = \frac{11}{6}\pi$ | $\theta_7 = \frac{1}{6}\pi$<br>$\theta_8 = \frac{1}{3}\pi$ |
| Material parameters (Shear modulus)[3] | Actin part | $\mu_a = 5$ | | | |
| | Epidermis part | $\mu_e = 1$ | | | |
| | Muscles | $\mu_m = 100$ | | | |
| | Soft inner part | $\mu_i = 1/200$ | | | |

[1] The radius are extracted or deduced by the Ref.(***Ben Amar et al.*** (***2018***); ***Lardennois et al.*** (***2019***)).
[2] The location and size of muscles are deduced by the Ref.(***Moerman and Williams*** (***2006***); ***Lardennois et al.*** (***2019***)).
[3] The units of the shear modulus are the $KPa$ and is scaled by the epidermis one. It gives for the muscle, a value consistent with the muscle shear modulus proposed in (***Denham et al.*** (***2018***)).

# Appendix 2

## Analytical model of the early elongation

The finite deformation gradient: $\mathbf{F}_0 = Diag(r'(R), r(R)/R, \lambda)$, and $\mathbf{G}_0 = Diag(1, g_0, 1)$, $0 < g_0 < 1$ in the actin layer, and $g_0 = 1$ in the part without actin budles. To determine the finite strain $\mathbf{G}_0$, we converted the four muscle parts into thin layers attached to the epidermis in equal proportions to ensure the continuity of the model, and divide our model into four parts, see Fig.1. The actin layer($R_3 < R < R_2{}'$), epidermis layer($R_2 < R < R_2{}'$) and muscle layer($R_1{}' < R < R_2$) are considered as incompressible materials, and the inner part($0 < R < R_1{}'$) is compressible. The Neo-Hookean energy function is used for the incompressible parts:

$$W = \mu \left[ \frac{1}{2} \left( Tr \left( \mathbf{F_e} \mathbf{F_e}^T \right) - 3 \right) - p \left( \det \mathbf{F_e} - 1 \right) \right], \tag{19}$$

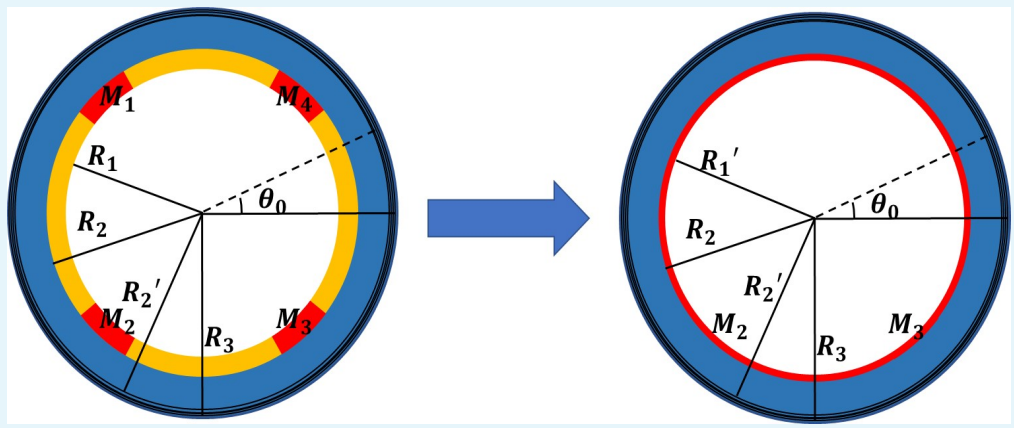


**Appendix 2—figure 1.** Cross-sectional simplified model with four scattered muscle sections simplified to thin layers ($R_1{}' = 0.768$).

According to the Euler-Lagrange equations, we can obtain the radius of actin layer($r_a$), epidermis layer($r_e$) and muscle layer($r_m$):

$$r_a = \sqrt{\frac{g_0 R^2 + A}{\lambda}}, \quad r_e = \sqrt{\frac{R^2 + E}{\lambda}}, \quad r_m = \sqrt{\frac{R^2 + M}{\lambda}}. \tag{20}$$

where A, E and M are constant, and the Lagrange multiplier $p$ in the actin, epidermis and muscle layer:

$$p_a = \frac{-\log(R) + \frac{1}{2} g_0{}^2 \left( -\frac{A}{A + g_0 R^2} + \log\left(A + g_0 R^2\right) \right)}{g_0 \lambda} + C_a, \tag{21}$$

$$p_e = -\frac{\frac{E}{E+R^2} + 2\log(R) - \log\left(E + R^2\right)}{2\lambda} + C_e, \tag{22}$$

$$p_m = -\frac{\frac{M}{M+R^2} + 2\log(R) - \log\left(M + R^2\right)}{2\lambda} + C_m. \tag{23}$$

For the compressible part, we take the energy function form (***Holzapfel*** (***2002***)):

$$W = \frac{\mu}{2} \left( Tr \left( \mathbf{F_e} \mathbf{F_e}^T \right) - 3 + \kappa \left( \det \mathbf{F_e} - 1 \right)^2 \right) \tag{24}$$

where $\kappa$ is a material constant. The radius of the inner part:

$$r_i = \frac{aR}{\sqrt{\lambda}} \tag{25}$$

where $a$ is a constant.

By considering the boundary condition $\sigma_{rr} = 0$ on the outer border $R = 1$:

$$\sigma_{arr}(R = 1) = \mu_a \left[ \left( \frac{\partial r_a(1)}{\partial R} \right)^2 - p_a(1) \right] = 0 \tag{26}$$

the continuity of the radius:

$$r_a(\mathrm{R}_2{}') = r_e(\mathrm{R}_2{}'), \quad r_e(\mathrm{R}_2) = r_m(\mathrm{R}_2), \quad r_m(\mathrm{R}_1{}') = r_i(\mathrm{R}_1{}'), \tag{27}$$

and the continuity of the radial stresses $\sigma_{rr}$ in $R_2{}'$ and $R_2$ :

$$\mu_a \left[ \left( \frac{\partial r_a(\mathrm{R}_2{}')}{\partial R} \right)^2 - p_a(\mathrm{R}_2{}') \right] = \mu_e \left[ \left( \frac{\partial r_e(\mathrm{R}_2{}')}{\partial R} \right)^2 - p_e(\mathrm{R}_2{}') \right], \tag{28}$$

$$\mu_e \left[ \left( \frac{\partial r_e(\mathrm{R}_2)}{\partial R} \right)^2 - p_e(\mathrm{R}_2) \right] = \mu_m \left[ \left( \frac{\partial r_m(\mathrm{R}_2)}{\partial R} \right)^2 - p_m(\mathrm{R}_2) \right]. \tag{29}$$

According to the above equations, we can obtain expressions for constants $E$, $M$, $C_a$, $C_e$ and $C_m$.

We substitute all size, material parameters and $\kappa = 100$, $\lambda = 1.8$ into the last condition $\sigma_{mrr}(\mathrm{R}_1{}') = \sigma_{irr}(\mathrm{R}_1{}')$:

$$\mu_m \left[ \left( \frac{\partial r_m(\mathrm{R}_1{}')}{\partial R} \right)^2 - p_m(\mathrm{R}_1{}') \right] = \mu_i \sigma_{irr}(\mathrm{R}_1{}'), \tag{30}$$

where $\sigma_{irr}$:

$$\sigma_{irr} = \frac{2}{\det \mathbf{F_e}} \left( (\det \mathbf{F_e})^2 \frac{\partial W}{\partial (\det \mathbf{F_e})^2} + \frac{\partial W}{\partial (tr(\mathbf{F_e}\mathbf{F_e}^T))} r_i{}'(R)^2 \right). \tag{31}$$

and obtain the relationship with constant $A$ and $g_0$.

Finally, by prescribing a zero traction condition on the top of the cylinder, noticeably, the muscle part was considered inextensible, so no stress on the top:

$$\int_{R_2{}'}^{1} \sigma_{azz} r_a r_a{}' dR + \int_{R_2}^{R_2{}'} \sigma_{ezz} r_e r_e{}' dR + \int_{0}^{R_1{}'} \sigma_{izz} r_i r_i{}' dR, \tag{32}$$

where:

$$\sigma_{azz} = \lambda^2 - p_a, \quad \sigma_{ezz} = \lambda^2 - p_e, \tag{33}$$

$$\sigma_{izz} = \frac{2}{\det \mathbf{F_e}} \left( (\det \mathbf{F_e})^2 \frac{\partial W}{\partial (\det \mathbf{F_e})^2} + \frac{\partial W}{\partial (tr(\mathbf{F_e}\mathbf{F_e}^T))} \lambda^2 \right), \tag{34}$$

all solutions $g_0 = 0.88$, $A = 0.08$ and $r_a(1) = 0.73$ can be determined. The result is also in good agreement with the experimental data (***Vuong-Brender et al.*** (***2017a***); ***Ben Amar et al.*** (***2018***)).

# Appendix 3

## Time-scale for myosin detachment

The time required for non-muscle myosin detachment is estimated to be $\tau_0 = 10s$ for free acto-myosin filaments. If the actin filament is submitted to external loading perpendicular to its axis, the detachment can be helped or on the contrary inhibited, see (***Howard and Clark*** (***2002***)), page 169-170. In the present case, the stresses acting in the radial direction of an actin bundle are compressive and thus will delay the detachment. This energy has to be compared to the energy of detachment of all myosin motors from the bundle. The corresponding elastic energy associated with the radial deformation for an actin cable of length $l_a$ of radius $r_b = 0.05\mu m$ estimated from (***Lardennois et al.*** (***2019***)) and shear modulus $\mu_a = 5\ KPa$ is given by $1/2\mu_a(1 - g_0(t))\pi l_a r_b^2 = 210^{-11} l_a\ J$. This result must be compared to the individual energy of detachment times the number of myosin motors on a cable. This number is uneasy to fix but estimation is given by the length of the cable $l_a$ divided by the distance between $2$ anchoring sites of myosin which is about $5nm$ while the attachment energy per motor is about $6k_bT$. These indications are for skeletal muscle myosins (***Howard and Clark*** (***2002***)) and have to be taken with caution. Nevertheless, the order of magnitude of the debonding energy for a collection of myosin heads from actin cable can be estimated to $4.8 l_a 10^{-12} J$. Then the ratio between both quantities is of order $4(1 - g_0(t))$ which explains that the time-scale of debonding for a cable in compressive stress in the orthogonal direction of its axis is then:

$$\tau_{deb} = \tau_0 e^{p_3(1-g_0(t))} \tag{35}$$

where $p_3$ is a positive constant of order one which cannot be predicted exactly. This time scale justifies the exponential correction in Eq.(3) of the manuscript.

# Appendix 4

## Modelling details of without pre-strain case

In the paper, we discuss the case with pre-strain. Here, more details about without pre-strain ($\mathbf{G_0} = \mathbf{I}$) case are displayed. To lowest order, the solution of the Euler–Lagrange equations is obviously given by $\mathbf{a}^{(0)} = (R, \Theta, 0)$, and $p^{(0)} = 1$ so there is no deformation and the zero and first order of energy vanish. At order $\mathcal{O}\left(\varepsilon^2\right)$ of the elastic energy, the solution for the active strain components are:

$$\begin{aligned} a_1^{(1)} &= -\frac{R}{2}\xi - \frac{R^2}{8}\left(u_1 \sin\Theta - u_2 \cos\Theta\right) + f_1(R), \\ a_2^{(1)} &= \frac{5R}{8}\left(u_1 \cos\Theta + u_2 \sin\Theta\right) + f_2(R), \\ a_3^{(1)} &= 0, \\ p^{(1)} &= f_3(R). \end{aligned} \tag{36}$$

where $f_{1,2}$ are functions related to the active stress $g$ and fiber angles $\alpha$ and $\beta$:

$$\begin{aligned} f_1(R) &= \frac{gR}{2}, \\ f_2(R) &= glog(R)\sin^2\alpha \sin(2\beta), \\ f_3(R) &= 2g\mu log(R)\sin^2\alpha \sin(2\beta). \end{aligned} \tag{37}$$

The coefficients for determining stiffness:

$$\begin{aligned} A_2 &= \frac{9\mu R}{8}, \\ B_2 &= \frac{81}{128}\mu R^3 \sin^2\Theta, \\ C_2 &= \frac{81}{128}\mu R^3 \cos^2\Theta, \\ D_2 &= \frac{\mu R^3}{2}. \end{aligned} \tag{38}$$

The coefficients for determining deformation:

$$\begin{aligned} A_1 &= -\frac{1}{8}g\mu R\left[4 + 5\cos(2\alpha) + 2\cos(2\beta)(-1 + 2\log(R))\sin^2\alpha\right], \\ B_1 &= -\frac{1}{16}g\mu R^2\left[10 + 17\cos(2\alpha) + 2\cos(2\beta)(-1 + 14\log(R))\sin^2\alpha\right]\sin\Theta, \\ C_1 &= \frac{1}{16}g\mu R^2\left[10 + 17\cos(2\alpha) + 2\cos(2\beta)(-1 + 14\log(R))\sin^2\alpha\right]\cos\Theta, \\ D_1 &= -g\mu R^2 \cos\beta \sin(2\alpha). \end{aligned} \tag{39}$$

## Modelling details of with pre-strain case

The first order solutions of the theory with the pre-strain case, $h_{1,2,3}(R)$ are related to activation $g$ and fiber angles $\alpha$ and $\beta$:

$$\begin{aligned} h_1(R) &= \frac{R(c+g)}{2\sqrt{\lambda}}, \\ h_2(R) &= g\log(R)\sin^2\alpha \sin(2\beta), \\ h_3(R) &= \frac{2\mu log(R)\left[c + g\cos(2\beta)\sin^2\alpha\right]}{\lambda}. \end{aligned} \tag{40}$$

The coefficients for determining stiffness:

$$
\begin{aligned}
A_2 &= (0.278 + 1.689\mu)\, R, \\
B_2 &= 1.294 R^3 \left[-0.405 + 2.389\mu + (-0.176 + \mu)\cos(2\Theta)\right], \\
C_2 &= -1.294 R^3 \left[0.405 - 2.389\mu + (-0.176 + \mu)\cos(2\Theta)\right], \\
D_2 &= 0.9\mu R^3.
\end{aligned}
\tag{41}
$$

The coefficients for determining deformation:

$$
\begin{aligned}
A_1 &= \mu R \Big[0.417c - 0.139g - 6.48g\cos^2\alpha - 0.556c\log(R) \\
&\quad + g\left(0.556\cos^2\beta - 0.556\cos(2\beta)\log(R)\right)\sin^2\alpha\Big]. \\
B_1 &= R^2 \Big\{g(-0.828 + 4.830\mu)\cos\beta\log(R)\sin^2\alpha\sin\beta\cos\Theta + 0.198c\sin\Theta \\
&\quad + \Big[0.198g + 0.910c\mu + 1.307g\mu - 4.830g\mu\cos^2\alpha - 1.225c\mu\log(R) \\
&\quad + g\mu\left(-0.397\cos^2\beta - 1.225\cos(2\beta)\log(R)\right)\sin^2\alpha\Big]\sin\Theta\Big\}. \\
C_1 &= R^2 \Big\{g(-0.828 + 4.830\mu)\cos\beta\log(R)\sin^2\alpha\sin\beta\sin\Theta - 0.198c\cos\Theta \\
&\quad + \Big[-0.198g - 0.910c\mu - 1.307g\mu + 4.830g\mu\cos^2\alpha + 1.225c\mu\log(R) \\
&\quad + g\mu\left(0.397\cos^2\beta + 1.225\cos(2\beta)\log(R)\right)\sin^2\alpha\Big]\cos\Theta\Big\}. \\
D_1 &= -g\mu R^2\cos\beta\sin(2\alpha).
\end{aligned}
\tag{42}
$$

# Appendix 5

## Energy transformation calculations

The energy transformation process is depicted in Fig.1.

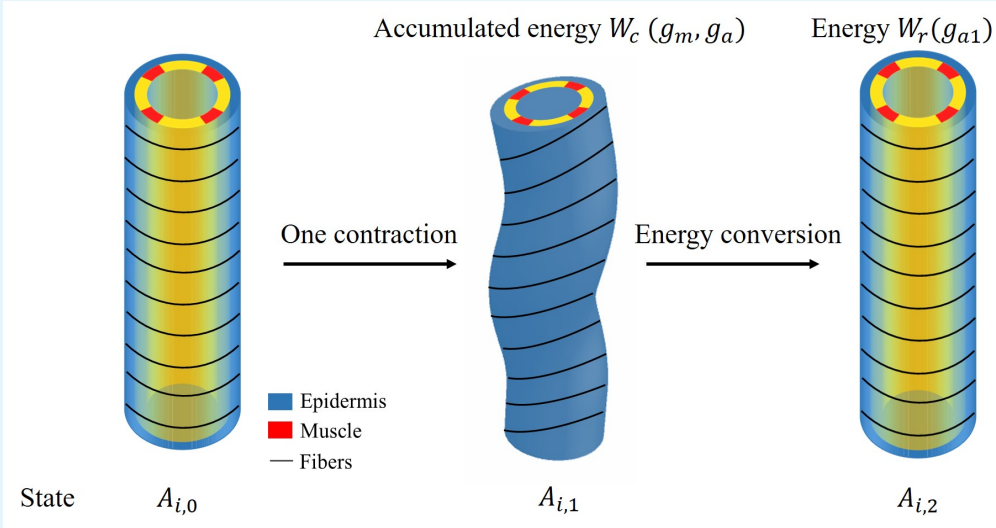


**Appendix 5—figure 1.** Schematic diagram of energy conversion.

To obtain the elongation $\delta\zeta_i$ after each muscle contraction, we need to calculate the energy, and the total energy takes the following form:

$$\mathcal{E} = \varepsilon^2 \int_0^L \mathrm{d}Z \int_S \left(V_0 + \varepsilon V_1 + \varepsilon^2 V_2\right) R\, \mathrm{d}R\, \mathrm{d}\Theta + O\left(\varepsilon^5\right) \tag{43}$$

where the integration region $S$ is related to each part of the cylinder with a different shear modulus $\mu$, so the model must be divided into 3 different parts for integration.

The final part of the energy conversion per unit volume is then:

$$\mathcal{E}_{\oint} = \int_S \left(\varepsilon V_1 + \varepsilon^2 V_2\right) R\, \mathrm{d}R\, \mathrm{d}\Theta \tag{44}$$

where $V_1$ is not the whole first order energy, we only consider the energy induced by activation of acto-myosin $g_a$ and muscles $g_m$. After obtaining solutions $\mathbf{a}^{(0)}$,$\mathbf{a}^{(1)}$ and deformations from Eq.(11)-(12), the accumulated energy during the contractile period $W_c$ that we define is:

$$\begin{aligned} W_c &= \int_S \left(\varepsilon V_1 + \varepsilon^2 V_2\right) R\, \mathrm{d}R\, \mathrm{d}\Theta \\ &= \varepsilon\left(-10.70 g_a - 7.73 g_m\right) + \varepsilon^2\left[\left(-3.31 + 26.75 g_a\right) g_a + 11.95 {g_m}^2\right]. \end{aligned} \tag{45}$$

When the muscles are relaxed and only acto-myosin is activated, the total increase of volumetric energy $W_r$ is then:

$$\begin{aligned} W_r &= \int_S \left(\varepsilon V_1 + \varepsilon^2 V_2\right) R\, \mathrm{d}R\, \mathrm{d}\Theta \\ &= -0.41 \varepsilon g_{a1} + \varepsilon^2\left(-5.19 + 6.96 g_{a1}\right) g_{a1}. \end{aligned} \tag{46}$$

By calculating energy conversion, we obtain $g_{a1} = -0.66$ at the beginning of the late elongation phase, Fig.7 of the manuscript shows the elongation for each contraction and total elongation varies with time.